

**Modelling of Badminton Shuttlecock Impact on  
Ground using Finite Element Analysis and Tensor  
Field Visualization**

by

**Sourabh Gopinath More**

A NON THESIS

submitted to

Oregon State University

in partial fulfillment of the requirements for the degree of

**Master of Science in Computer Science**

Presented December 2025

Corvallis, Oregon

*Master of Science non-thesis of Sourabh Gopinath More presented on*

December 08, 2025

**APPROVED:**

---

Major Professor, representing Computer Science

---

Head of the School of Electrical Engineering and Computer Science

---

Dean of Graduate Education

I understand that my project will become part of the permanent collection of Oregon State University libraries. My signature below authorizes release of my project to any reader upon request.

---

Sourabh Gopinath More, Author

## **ACKNOWLEDGEMENTS**

*I would like to express my deepest appreciation to my parents for their endless encouragement, patience, and belief in my abilities. Their constant motivation and unconditional support have been the foundation of every step I have taken in this journey. Their sacrifices and faith in my goals have given me the strength and determination to persist through every challenge.*

*I am also sincerely thankful to my advisor, Dr. Yue Zhang, for her invaluable guidance, thoughtful insights, and continuous mentorship throughout this work. Her dedication, constructive feedback, and generosity with time and knowledge have greatly shaped both the technical and personal growth I experienced during this research. This project stands as a reflection of her lasting influence and support.*

## Abstract

The unique combination of geometry, material heterogeneity, and rapid changes in contact force for the badminton shuttlecock cause it to behave in a manner that cannot be easily described by simple analytical or semi-analytical means. A simulation of such interactions (and therefore a way to analyze them) was made possible by the use of Finite Element Modeling (FEM) techniques used in this project to model the dynamic impact behavior of both the nylon and feather badminton shuttlecocks after they have been dropped from free fall.

This research developed models based on 3D geometric representations of the shuttlecocks created in Blender and meshed at a level of detail suitable for simulating high rate impacts. In addition, these models were designed to include detailed descriptions of the materials used to build the shuttlecocks, along with appropriate boundary conditions and contact formulations to accurately describe how stress, strain and deformation occur within milliseconds of when the shuttlecocks strike the floor. In the models presented, the cork head of the shuttlecock was represented as a linear elastic solid, the feathers were represented as isotropic elastic elements and the nylon skirt was represented using linear elastic properties consistent with polymer behavior.. The rigid floor was represented as a reference surface that does not move and has fixed boundary conditions applied to it. Each shuttle was subject to gravitational loads and free-fall impact to simulate the experimental conditions.

Validation of the numerical model was performed through convergence studies, solver cross-validation using Siemens NX and Abaqus, and field validation using tensor quantities extracted from stress and strain data. Additionally, visualization of

the tensor fields provided insight into the directional development of the individual stress components which enabled a better understanding of how the load transfer and deformation propagates throughout the shuttle structure during the contact and rebound phases. Accuracy of the models was also validated by monitoring the energy balance, time-step stability and contact consistency for both shuttle types.

Analysis demonstrates two distinct types of mechanical properties exhibited by the nylon and the feather shuttlecocks. The feather shuttlecock has an extremely rapid loss of energy, and this is caused by localized flexing at the feather to head area. Localized flexing creates additional energy absorption by the feathers at the time of impact, which results in significantly reduced rebound height and more rapid decrease in motion with each subsequent bounce.

Conversely, the nylon shuttlecock distributes stress throughout its entire length of continuous skirt allowing for much better storage of and return of energy with respect to higher bounce heights and less irregular rebound profiles. The geometry and material stiffness of nylon allow the energy to spread across a larger region, resulting in smoother rebound.

The above conclusions are valid for the ranges of simulated impact energy associated with low to moderate playing speeds, where both material exhibit elastic limit properties. In summary, this research established a validated continuum mechanics based simulation tool to provide objective comparisons and interpretations of the impact behavior of the nylon and feather shuttlecocks.

## Acknowledgements

# Contents

<b>Abstract</b>	ii
<b>Acknowledgements</b>	iii
<b>1 Introduction</b>	1
1.1 Motivation . . . . .	3
<b>2 Background</b>	6
2.1 Continuum Mechanics . . . . .	6
2.2 Material Modeling . . . . .	9
2.2.1 Linear Materials vs Nonlinear Materials . . . . .	11
2.2.2 Geometry Shapes . . . . .	12
2.2.3 Composition (Connectivity and Compatibility at Interfaces) .	13
2.2.4 Numerical Modeling (Procedures Used) . . . . .	16
2.3 Interfaces of Different Parts . . . . .	17
2.3.1 Rubber Head–Feather Interface (Shuttle Assembly) . . . . .	17
2.3.2 Interface Challenges . . . . .	19

2.4	Scalar Fields in Computational Simulation . . . . .	23
2.5	Vector and Tensor Fields in Computational Mechanics . . . . .	24
<b>3</b>	<b>3D Modeling of Shuttlecock in Blender</b>	<b>25</b>
3.1	Modeling Strategy and Unit Configuration . . . . .	25
3.2	Feather Shuttlecock Geometry . . . . .	26
3.2.1	Cork Head . . . . .	26
3.2.2	Feather Array . . . . .	26
3.2.3	Adhesive Skirt Rim . . . . .	27
3.3	Nylon Shuttlecock Geometry . . . . .	29
3.3.1	Head and Interface Region . . . . .	29
3.3.2	Polymer Skirt . . . . .	30
3.4	Export and Pre-Processing for Simulation . . . . .	30
3.5	Summary . . . . .	32
<b>4</b>	<b>Meshing Strategy and Material Parameters</b>	<b>34</b>
4.1	Unit System . . . . .	34
4.2	Global Meshing Policy . . . . .	36
4.3	Feather Shuttle – Mesh and Elements . . . . .	37
4.4	Nylon (Plastic) Shuttle – Mesh and Elements . . . . .	39
4.5	Material Properties and Assignments . . . . .	41
4.6	Remarks on Mesh Adequacy . . . . .	44
4.7	Boundary Conditions and Simulation Setup . . . . .	44
4.7.1	Floor Definition . . . . .	44
4.7.2	Shuttle Definition . . . . .	45

4.7.3	Contact Interaction . . . . .	45
4.7.4	Simulation Setup . . . . .	46
4.8	Simulation Parameters Summary . . . . .	48
4.9	Connection to and Validation against Continuum Mechanics . . . . .	51
<b>5</b>	<b>Numerical Convergence and Accuracy</b>	<b>55</b>
5.1	What numerical convergence means . . . . .	55
5.2	What numerical accuracy means . . . . .	56
5.3	Convergence control . . . . .	56
5.3.1	Mesh refinement . . . . .	57
5.3.2	Time-step refinement . . . . .	59
5.4	Accuracy control . . . . .	61
5.4.1	Contact and interface choices . . . . .	61
5.4.2	Element Formulations . . . . .	61
5.4.3	Material Model Choices . . . . .	62
5.4.4	Numerical Stability Enhancements . . . . .	62
5.5	Implicit and Explicit Dynamic Procedures . . . . .	63
<b>6</b>	<b>Results</b>	<b>66</b>
6.1	Energy Response of the Feather Shuttle . . . . .	66
6.2	Energy Response of the Nylon Shuttle . . . . .	72
6.3	Bounce Height Analysis . . . . .	78
6.4	Bounce Angle Analysis . . . . .	86
6.5	Dynamic Implicit vs. Dynamic Explicit Comparison . . . . .	98
6.6	Mises Stress Analysis in Shuttlecock Cork . . . . .	102

6.6.1	Feather Shuttle Cork . . . . .	102
6.6.2	Nylon Shuttle Cork . . . . .	103
6.7	Velocity Response Analysis . . . . .	105
6.7.1	Velocity of the Feather Shuttle . . . . .	105
6.7.2	Velocity of the Nylon Shuttle . . . . .	106
6.7.3	Comparison of Velocity Response . . . . .	107
6.8	Simulation Performance and Computational Time . . . . .	109
<b>7</b>	<b>Tensor Field Visualizations</b>	<b>112</b>
7.1	Overview . . . . .	112
7.2	Tensor Field Visualizations for Shuttle Corks Immediately Before Contact . . . . .	113
7.3	Tensor Field Visualizations for Shuttle Corks at Contact . . . . .	115
7.4	Tensor Field Visualizations for Shuttle Corks Immediately after Contact	117
<b>8</b>	<b>Conclusion</b>	<b>120</b>
8.1	Summary of Findings . . . . .	120
8.1.1	Feather Shuttle . . . . .	120
8.1.2	Nylon Shuttle . . . . .	122
8.2	Comparative Discussion . . . . .	123
8.3	Overall Conclusion and Future Scope . . . . .	124
8.4	Application: VR Badminton Game . . . . .	125
<b>References</b>		<b>132</b>

# List of Figures

2.1	Cork head model created in Blender, representing the rigid impact component in the shuttlecock assembly. . . . .	14
2.2	Modeled feather element in Blender showing the shaft and vane geometry used to construct the finite element mesh. This geometry serves as the basis for the material modelling of the feather, where the keratin structure is approximated using a lightweight linear elastic model suitable for impact analysis. . . . .	15
2.3	Assembly of the shuttlecock sub-components created in Blender. Each feather shaft is placed in between an outer ring that surrounds the cork head, reflecting the construction used in commercial feather shuttlecocks. This geometric connection establishes how each feather is physically joined to the head before any material models or interface constraints are applied in the finite element setup. . . . .	15
3.1	Thin polymer ring . . . . .	27
3.2	Feather shuttlecock - bottom view . . . . .	28
3.3	Feather shuttlecock - side view . . . . .	28
3.4	Feather shuttlecock - top view . . . . .	29
3.5	3D modeled feather shuttlecock from different orientations in Blender.	29

3.6	Nylon (plastic) shuttlecock - bottom view . . . . .	31
3.7	Nylon (plastic) shuttlecock - side view . . . . .	31
3.8	Nylon (plastic) shuttlecock - top view . . . . .	32
3.9	3D modeled nylon (plastic) shuttlecock from different orientations in Blender. . . . .	32
4.1	Finite element mesh of the feather shuttle model showing tetrahedral (C3D4) elements distributed over the skirt and cork head. . . . .	38
4.2	Finite element mesh of the Nylon shuttle model showing tetrahedral (C3D4) elements distributed over the skirt and cork head. . . . .	40
4.3	Sliced structural and material views illustrating the feather–cork interface. These visuals show how the feather shafts are placed in between the supporting ring above the cork head and how material properties are assigned in the finite element model. The feather elements (green) are modeled using a lightweight linear elastic material, while the cork head (red) is modeled using a compressible elastic material to accommodate impact deformation. . . . .	43
4.4	Boundary conditions and simulation setup for shuttle free-fall analysis.	47
6.1	Internal energy variation of the feather shuttle. . . . .	67
6.2	Kinetic energy variation of the feather shuttle. . . . .	69
6.3	Combined kinetic and internal energy of the feather shuttle. . . . .	71
6.4	Internal energy variation of the nylon shuttle. . . . .	73
6.5	Kinetic energy variation of the nylon shuttle. . . . .	75
6.6	Combined kinetic and internal energy of the nylon shuttle. . . . .	77

6.7	Rebound height variation of the feather shuttle for five successive bounces. . . . .	81
6.8	Rebound height variation of the nylon shuttle for three successive bounces. . . . .	83
6.9	Comparison of bounce height variations between feather and nylon shuttles. . . . .	85
6.10	Orientation of the shuttlecock at impact. The center of mass is aligned vertically, forming a $90^\circ$ angle with the floor, which is used as the reference configuration for bounce-angle analysis. . . . .	87
6.11	Shuttlecock orientation at a $45^\circ$ impact angle relative to the floor, illustrating an off-axis approach trajectory used for bounce-angle comparison.	88
6.12	Shuttlecock orientation at a $0^\circ$ angle, with the feathers nearly parallel to the floor, representing the extreme case of a horizontal or near-horizontal impact. . . . .	89
6.13	Bounce angle variation of the feather shuttle across five rebounds. . . . .	93
6.14	Bounce angle variation of the nylon shuttle across three rebounds. . . . .	95
6.15	Comparison of bounce angle variation between feather and nylon shuttles. . . . .	97
6.16	Von Mises stress in the feather shuttle cork during Bounce 1 (left) and Bounce 5 (right). . . . .	103
6.17	Von Mises stress in the nylon shuttle cork during Bounce 1 (left) and Bounce 3 (right). . . . .	104
6.18	Velocity magnitude distribution in the feather shuttle for the first and fifth rebounds. . . . .	106

6.19	Velocity magnitude distribution in the nylon shuttle for the first and third rebounds.	107
7.1	Tensor-field degeneracy curves on the shuttle corks immediately before ground contact during Bounce 1. Top row: feather shuttle; bottom row: nylon shuttle. Yellow curves denote planar degeneracies and green curves denote linear degeneracies.	114
7.2	Tensor-field degeneracy curves on the shuttle corks during the first contact. Top row: feather shuttle (top and side views); bottom row: nylon shuttle (top and side views). Yellow curves denote planar degeneracies; green curves denote linear degeneracies.	116
7.3	Tensor-field degeneracy curves on the shuttle corks immediately after ground contact during Bounce 1. Top row: feather shuttle; bottom row: nylon shuttle. Yellow curves denote planar degeneracies and green curves denote linear degeneracies.	118
8.1	Frames from the developed VR badminton environment showing in-game interaction and Unity-based scene setup.	129

## List of Tables

4.1	Global coordinate system and unit conventions used in all simulations.	35
4.2	Summary of finite element formulations used for each model component.	36

4.3	Constitutive parameters used in the models (native units m–kg–s–N; SI density shown for reference). . . . .	41
4.4	Detailed material focus describing constitutive model, physical behavior, and element assignment for each component. . . . .	42
4.5	Summary of input and solver parameters used in shuttle free-fall simulations. . . . .	49
4.6	Summary of numerical controls and solver settings adopted for explicit dynamic simulations. . . . .	50
4.7	Verification checklist used to ensure numerical stability and accuracy. . . . .	54
5.1	Mesh refinement comparison for the feather shuttle under free-fall impact. QoIs stabilize between coarse and fine meshes, indicating mesh-independent behavior. . . . .	58
5.2	Time-step sensitivity study for the feather shuttle. Reducing the explicit time increment by 25% produces only minor changes in QoIs. . . . .	59
5.3	Convergence parameters and target acceptance criteria used in refinement studies. . . . .	60
5.4	General comparison of implicit and explicit dynamic procedures. . . . .	64
6.1	Measured rebound heights of feather and nylon shuttles under free-fall from 14 mm. . . . .	79
6.2	Measured bounce angles of feather and nylon shuttles during free-fall impact. . . . .	91
6.3	Comparison of first three bounce heights between Dynamic Explicit and Dynamic Implicit analyses. . . . .	99

6.4	Comparison of rebound angles for the first three bounces. . . . .	99
6.5	Comparison of energy (ALLKE) for the first three bounces. . . . .	99
6.6	Comparison of energy (ALLIE) for the first three bounces. . . . .	100
6.7	Comparison of velocity response for feather and nylon shuttles. . . . .	108
6.8	Simulation performance summary for feather and nylon shuttle free-fall analyses. . . . .	111
7.1	Simplified comparison of degeneracy-curve behavior across pre-impact, impact, and post-impact frames. . . . .	119
7.2	Step time and number of degeneracy curves for feather and nylon shuttle corks across pre-impact, impact, and post-impact frames. . . . .	119

# 1. Introduction

Understanding the mechanical behavior of a badminton shuttlecock during impact is essential for improving its aerodynamic stability, structural durability, and overall performance. The shuttle experiences rapid deformation, high strain rates, and transient contact events that occur within milliseconds of impact. Experimental approaches often face limitations in resolving these effects with sufficient temporal or spatial precision. Finite Element Analysis, rooted in continuum mechanics, provides a robust framework to study these complex interactions by capturing stress propagation, strain localization, and material response under realistic loading conditions.

This project presents a computational study of shuttlecock impact dynamics based on continuum mechanics principles using Siemens NX and Abaqus software. The research investigates two primary scenarios: the free fall of a feather shuttlecock onto a rigid floor and the free fall of a nylon shuttlecock under identical conditions. Both simulations are designed to quantify deformation behavior, stress concentration, contact forces, energy dissipation, and rebound characteristics during impact. The goal is to establish a reliable numerical foundation for understanding shuttle performance under controlled impact conditions.

The shuttlecock models are constructed as detailed three-dimensional representations that replicate the geometry of actual shuttles. Each model consists of a cork or rubberized head and a surrounding skirt composed of either natural feathers or polymer material. Material properties are defined according to the dominant mechanical response of each component. The cork head is modeled as a linear elastic

solid, the feathers are represented using isotropic elastic parameters, and the nylon skirt is characterized using linear elastic polymer properties. These definitions ensure that the simulated response aligns with realistic mechanical behavior during impact.

Special emphasis is placed on defining appropriate boundary conditions, contact algorithms, and mesh refinement strategies to ensure stability and accuracy in numerical solutions. The explicit dynamic solver in Abaqus is used to capture the transient response of high-speed impact, while complementary simulations in Siemens NX are performed for verification and consistency. The dual-platform approach ensures that the results are independent of solver-specific numerical artifacts.

The analysis produces detailed visualizations and quantitative results, including Cauchy and von Mises stress distributions, displacement contours, contact force histories, and energy-time evolution during impact. The feather shuttlecock exhibits localized bending and stress concentration near the feather–head interface, while the nylon shuttle shows broader stress diffusion due to its properties. These findings demonstrate the influence of geometry and material composition on impact response and energy absorption.

Finally, the study addresses numerical convergence, time-step sensitivity, and energy balance to confirm the reliability of the computational framework. The outcomes provide a validated finite element methodology for modeling shuttlecock impacts and contribute to the broader understanding of shuttle dynamics. The results can serve as a foundation for further design optimization, material selection, and performance evaluation of badminton shuttlecocks in future studies.

## 1.1 Motivation

Badminton is a sport defined by speed, precision, and the complex flight behavior of the shuttlecock. Each strike during play produces rapid deformation, high strain rates, and transient contact between the shuttle and the surrounding environment. The shuttlecock is a composite structure made from materials that differ greatly in stiffness and density, which makes its response highly sensitive to geometry and loading. Understanding this mechanical behavior requires an advanced computational approach that can capture large deformations, rate-dependent material effects, and nonlinear contact interactions with physical accuracy. Conventional experiments or video-based observations are often unable to resolve the fast stress propagation and localized energy dissipation that occur within milliseconds of impact.

This research is driven by the need to develop a physically consistent and computationally validated model of shuttlecock impact behavior using principles of continuum mechanics and the finite element method. The objective is to study how material composition and geometry influence deformation, rebound, and energy transfer when the shuttle impacts a rigid surface. The investigation focuses on two representative cases: the free fall of a feather shuttlecock and the free fall of a nylon shuttlecock. Both cases are designed to reveal how energy is stored, dissipated, and released during impact under identical boundary conditions.

A practical motivation also arises from the high cost and limited durability of shuttlecocks used in professional and recreational play. On average, two dozen shuttlecocks are consumed in a single olympic match, and frequent replacement adds significant expense for players and tournament organizers. Feather shuttles, in par-

ticular, are costly to produce and degrade quickly due to moisture absorption and repeated impact loading. To address this issue, the study aims to contribute toward the design of a more durable shuttlecock made from alternative materials that can replicate the mechanical and aerodynamic performance of tournament-grade designs while offering improved longevity and affordability.

From a scientific perspective, this research extends the application of finite element analysis to a complex system composed of multiple materials with distinct mechanical behaviors. The cork head, feather skirt, and polymer skirt exhibit different elastic responses, requiring precise element formulations to represent each region accurately. Through this modeling framework, the study integrates structural mechanics, contact analysis, and numerical convergence verification to ensure that results are both physically meaningful and computationally stable.

The broader aim of this work is to establish a computational foundation for future studies on shuttlecock performance and material optimization. By linking material behavior, geometry, and impact response, the research provides a deeper mechanical understanding of shuttle dynamics that can inform future design improvements. Such a framework has potential applications in both manufacturing and sports engineering, leading to the development of shuttlecocks that are more consistent, durable, and cost-effective for use in competitive badminton.

Beyond the analytical scope, this project also emphasizes the visualization and interpretation of numerical data obtained from finite element simulations. Outputs such as deformation profiles, contact pressure maps, and energy dissipation patterns are processed to extract statistical quantities including mean stress, rebound velocity, coefficient of restitution. These quantitative metrics serve as validation parameters

and as a dataset for further simulation-driven applications. The visualization component, developed using high-quality graphical representations, bridges the gap between abstract numerical results and physically interpretable behavior.

Finally, the research connects computational mechanics with modern visualization technologies to promote the development of interactive and data-driven sports simulations. The numerical dataset produced through this work can serve as a foundation for creating physics-based visual models that accurately reproduce the behavior of shuttlecock impacts. This integration of numerical modeling, graphical analysis, and material research represents a step toward combining engineering simulation with realistic virtual environments for the advancement of sports technology.

## 2. Background

### 2.1 Continuum Mechanics

The shuttlecock is a lightweight structure with a highly deformable geometry, and its response during impact is governed by a combination of complex material behavior and rapid changes in contact force. When the shuttle strikes a rigid floor, the load is transferred almost entirely through the cork head and the lower region of the skirt. This produces a sharp, concentrated impulse that causes the cork to compress, the feathers or nylon skirt to bend, and the entire structure to experience transient deformation waves that travel through the shuttle within a very short time.

Modeling this behavior requires a continuum mechanics framework capable of representing both the local material response and the global deformation pattern. The cork behaves as an elastic solid with relatively high stiffness, while the feather and nylon components respond through bending, stretching, and shear. The rapid impact generates large deformation gradients, and the geometry of the shuttle amplifies this effect by distributing the load through thin, flexible members. Capturing these mechanisms in a simulation environment involves relating the constitutive behavior of each material to the overall dynamic motion of the shuttlecock, including its energy absorption, rebound characteristics, and temporary loss of structural alignment after impact. Through this framework, the numerical model can replicate how the shuttle deforms, stores energy, and recovers shape during each bounce.

Continuum mechanics is a fundamental branch of mechanics that models materials as continuous, infinitely divisible media, even though their actual structure is

made up of discrete particles at the atomic or molecular scale. The continuum assumption enables the description of mechanical behavior using smooth, differentiable fields for quantities such as displacement, stress, and strain, defined at every point within the body. This abstraction is not merely a mathematical convenience - it is a necessity when dealing with engineering-scale systems, where resolving individual atomic interactions is neither practical nor computationally feasible.

In this research, continuum mechanics provides a physical and mathematical foundation for simulating the badminton shuttlecock as a deformable solid. Instead of tracking the motion of individual atoms, the shuttlecock is represented as a continuous body whose mechanical properties such as Young's modulus, Poisson's ratio, and density are spatially uniform or vary in a controlled manner for different materials. This approach allows the governing equations of motion to be expressed in terms of continuous field variables, making it possible to capture the deformation, stress development, and energy transfer within the shuttlecock under external loading in a computationally efficient and physically meaningful way.

The governing framework is built upon three fundamental conservation principles:

**Conservation of Mass** - The total mass of the body remains constant throughout deformation and motion. Mathematically, the density of the material and the volume changes are related through the continuity equation.

**Conservation of Linear and Angular Momentum** - The net force and net moment acting on a body equal the rate of change of its linear and angular momentum. These laws give rise to the balance of momentum equations, which in turn lead to the Navier-Cauchy equations for solid mechanics.

**Conservation of Energy** - The change in internal energy is equal to the work done by external forces plus any heat transfer, ensuring thermodynamic consistency in mechanical modeling.

Deformation is quantified using strain measures, which describe how distances, angles, and volumes change under loading. The most common measure in small-deformation analysis is the engineering strain, whereas large-deformation problems require nonlinear measures like the Green-Lagrange strain tensor. The internal resistance to deformation is expressed through stress measures, with the Cauchy stress tensor being the most physically intuitive as it directly relates the force acting on a surface to the orientation of that surface.

In practical computational mechanics, the presence of complex geometries of badminton shuttlecock makes analytical solutions infeasible. These shapes introduce irregular boundaries and nonlinear contact conditions that conventional integrations cannot resolve. Consequently, the governing laws are expressed as partial differential equations (PDEs) that require numerical treatment.

The Finite Element Method (FEM) provides the framework that makes these PDE problems tractable. By discretizing a continuous geometry into finite elements, FEM approximates the governing equations with shape functions, transforming the PDEs into a system of algebraic equations solvable by a computer.

In Siemens NX, this formulation is implemented through an integrated pre-processor, solver, and post-processor. The software computes displacement fields, stress distributions, and strain patterns at each element and node of the mesh, enabling point-by-point evaluation of the structure's behavior under dynamic loading. In parallel, I also use Abaqus - specifically Abaqus/Explicit for high-rate events such

as shuttle free-fall and impact, and Abaqus/Standard for quasi-static checks when needed. The same continuum formulation is advanced in time with either an explicit central-difference scheme (stable for severe contact and large deformation) or an implicit scheme (robust for equilibrium problems). Geometry, mesh, contacts, and loads are defined in the `.inp` model, and results are stored in the `.odb` database for post-processing. This dual-solver setup lets me cross-validate responses under identical boundary conditions and material definitions, and it helps separate modeling choices from solver-specific numerical artifacts (e.g., mass scaling, bulk viscosity, or hourglass control in explicit dynamics). In this project, continuum mechanics serves as the foundation for simulating high-impact scenarios on the rigid floor and for interpreting the resulting Cauchy stress distributions in a way that reflects real-world mechanical performance.

## 2.2 Material Modeling

In this work, the material behavior of the shuttlecock is defined according to the function of each component and its corresponding strain and rate regime, allowing the solver to capture responses that are both realistic and numerically stable. The cork head is modeled as a linear elastic material because it primarily deforms within the small strain range where stress and strain maintain a path independent relationship. This assumption ensures a stable and physically consistent response under impact loading. The feathers are represented using Isotropic elastic properties. This approach allows the model to replicate bending and twisting of the feather shafts during impact and rebound, where local stiffness and fiber orientation significantly influence the overall deformation pattern. Together, these elastic formulations define the structural

rigidity and recovery behavior of the natural shuttlecock components.

The nylon skirt exhibits a distinctly different mechanical response characterized by large recoverable deformations, nonlinear stress-strain behavior, and strong dependence on strain rate. To represent these effects, it is modeled as a linear elastic material with an explicit strain energy function. The material is treated as nearly incompressible, with the Poisson ratio close to 0.39, and an appropriate bulk modulus is selected to control volumetric deformation. The parameters for this model are calibrated using available material data and validated against the rebound and energy loss observed in simulations. These constitutive representations allow the analysis to reproduce realistic deformation modes, stress propagation, and energy transfer in both feather and nylon shuttlecocks.

The shuttlecock is modeled as a multi-material structure, with each component assigned mechanical properties consistent with its physical behavior. The head or nose undergoes the largest localized compression during impact and therefore is represented using a linear elastic material with a sufficiently high bulk modulus to control volumetric deformation. Linear tetrahedral solid elements are used in the head region to avoid volumetric locking and ensure accurate stress calculations. In feather shuttlecocks, the cork core is defined as a linear elastic solid, while the thin outer cap, typically made of a polymer or rubber-like material is also modeled using a linear elastic formulation to capture its small-strain impact response. In nylon shuttlecocks, the skirt behaves as a flexible polymer lattice and is assigned linear elastic properties consistent with nylon-based materials used in commercial shuttlecocks. The feathers, composed of keratin shafts and vanes, are slender structures dominated by bending stiffness. They are modeled using isotropic linear elastic properties. Together, these

material definitions allow the simulation to capture the essential deformation modes and stress transfer pathways during shuttlecock impact.

These material definitions establish a coherent and physically meaningful representation of shuttlecock behavior across the different components. Each constitutive model corresponds to the observed strain and strain rate range, ensuring numerical stability and physical consistency while allowing the results to be validated against controlled experimental or reference data.

### 2.2.1 Linear Materials vs Nonlinear Materials

In this project, the terms linear and nonlinear refer to how the material responds to deformation and whether the stress-strain relationship depends on the magnitude of strain or on changes in geometry during loading. A linear material exhibits a proportional and path independent relationship between stress and strain within the relevant deformation range. Its stiffness remains constant throughout loading, and in the small strain setting, the constitutive behavior is fully defined by constants such as Young's modulus and Poisson's ratio for isotropic solids, or by direction-dependent stiffness components in the case of orthotropic materials. Linear elasticity is computationally efficient and is appropriate when the material experiences only moderate deformation and the intrinsic material response does not change with strain amplitude.

Nonlinearity in this study arises only from geometric effects (deformations or rotations), not from the material law. Even though all components of the shuttlecock are modeled using linear elastic constitutive equations, the structure undergoes large rotations, bending, and contact-induced deformation that cause the response to

become geometrically nonlinear. This means the stiffness matrix must be updated as the configuration evolves, even though the underlying stress-strain relationship remains linear. The polymeric regions of the shuttlecock, including the nylon skirt and the outer cap on the cork head, are treated as linear elastic materials as well, since the impact conditions in this study remain within strain levels where a linear approximation is adequate. The cork head and the feathers similarly operate within the small strain regime, making linear elasticity an appropriate and stable choice.

By distinguishing between material linearity and geometric nonlinearity, the simulation maintains numerical efficiency while still capturing the key deformation mechanisms that govern shuttlecock impact behavior.

### 2.2.2 Geometry Shapes

Geometry dictates both the governing mechanics and the appropriate element types. Curved frames carry bending and torsion; modeling them with solid elements or curved beam/shell representations preserves stiffness coupling between directions. Straight, slender members (feather shafts) are dominated by axial and bending behaviors; beam or truss/cable elements capture their physics economically, provided the slenderness (length-to-diameter) is high and cross-sections are well defined. Thin wires vs flat beams differ primarily in shear and bending response: cables/trusses transmit only axial tension (ideal for tension-only strings), while beams transmit bending and shear (appropriate for feathers or any string segment expected to contact or press against constraints). Sphere/hemispherical caps (shuttle head) concentrate contact pressures and, for rubber-like caps, require near-incompressible solid elements to avoid volumetric locking. Membranes (homogenized nets) carry in-plane tension

with negligible bending stiffness; they are ideal when the woven micro-structure is not resolved. Finally, continuum vs discrete representations trade fidelity for cost: a continuum membrane reproduces effective bed stiffness and pre-tension well with few degrees of freedom, whereas a discrete string lattice is necessary to study crossing friction, local stick-slip, or grommet interactions. In this project, I use the simplest geometric representation of the shuttlecock that still captures the physical behavior relevant to the study—specifically the impact forces, deformation patterns, and rebound characteristics.

### 2.2.3 Composition (Connectivity and Compatibility at Interfaces)

The assembly is a composite system whose parts must move coherently at their junctions. “Who connects to whom?” The shuttlecock is a composite structure whose parts must deform and move together in a physically consistent manner at their junctions. The feather shafts are placed in between the outer ring that surrounds the cork head, and the head itself interacts directly with the rigid floor during impact. Compatibility in this context means that at bonded regions, the displacement field remains continuous without any gaps or overlaps, and the traction across the interface maintains equilibrium. Where relative motion is allowed, compatibility is maintained only in the normal direction to prevent penetration, while tangential movement follows a frictional sliding law that defines the interaction between surfaces. Numerically, compatibility is achieved through tied or coupled constraints where no slip is intended, such as at the interface between the feather roots and the head. Surface contact definitions are applied where sliding or separation is physically expected, for example

along the outer surface of the head during impact. Cohesive or connector-based interactions are introduced when gradual separation, pullout, or localized detachment is studied. After each simulation setup, the model is verified to ensure that reaction forces across all interfaces are balanced, that overclosure remains within acceptable limits, and that energy transfer across contact zones is smooth and free from numerical instability or artificial oscillations.

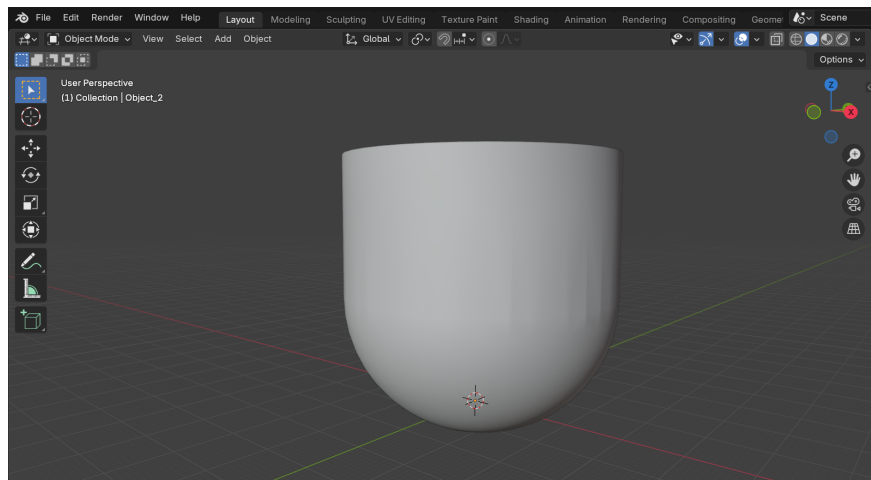


**Figure 2.1:** Cork head model created in Blender, representing the rigid impact component in the shuttlecock assembly.

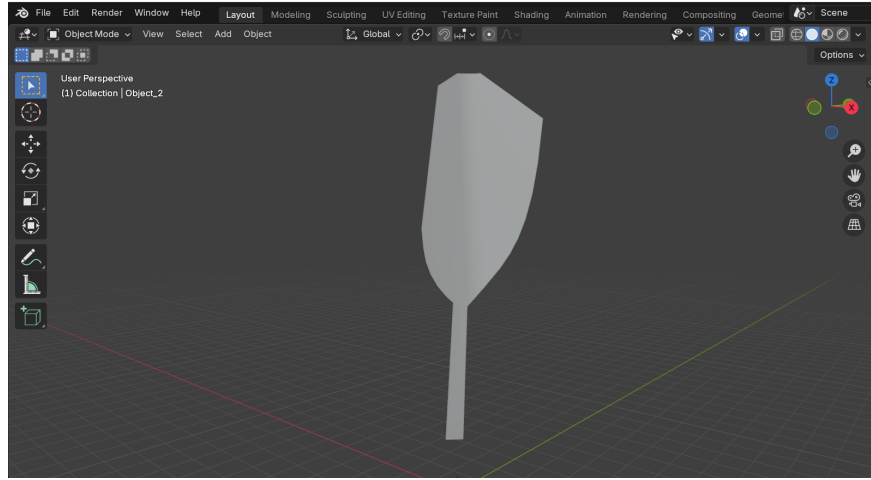


**Figure 2.2:** Modeled feather element in Blender showing the shaft and vane geometry used to construct the finite element mesh. This geometry serves as the basis for the material modelling of the feather, where the keratin structure is approximated using a lightweight linear elastic model suitable for impact analysis.

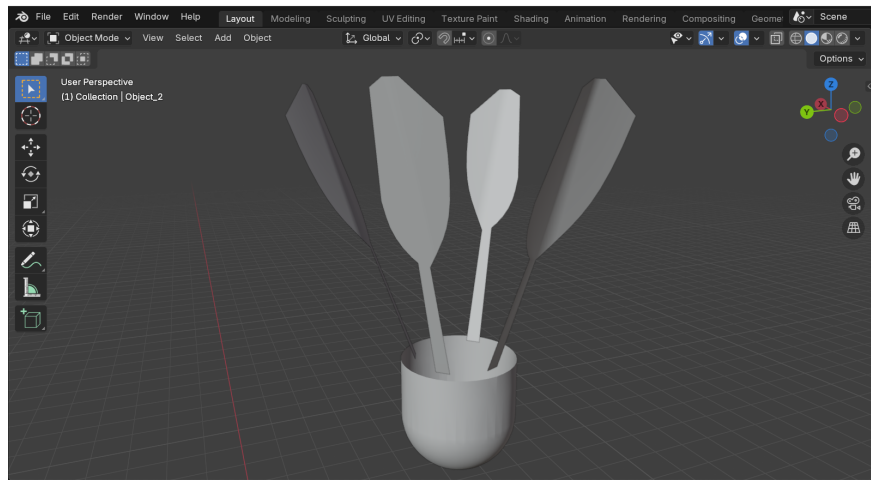


**Figure 2.3:** Assembly of the shuttlecock sub-components created in Blender. Each feather shaft is placed in between an outer ring that surrounds the cork head, reflecting the construction used in commercial feather shuttlecocks. This geometric connection establishes how each feather is physically joined to the head before any material models or interface constraints are applied in the finite element setup.

## 2.2.4 Numerical Modeling (Procedures Used)

This subsection summarizes the numerical procedures used in the simulations so that the analysis can be reproduced by another researcher.

- (1) **Units and material data.** A single, consistent unit system was used throughout the model. All components were assigned linear elastic material properties. The cork head was modeled as an isotropic elastic solid, the feathers were assigned isotropic elastic properties, and the nylon skirt was represented using linear elastic data obtained from manufacturer specifications and published mechanical property ranges.
- (2) **Geometry idealization.** The cork head was represented as a solid body, while the feather structures were modeled based on their simplified 3D profiles. The feather shaft and vane regions were idealized using thin structural members. Junctions between components were smoothed with small fillets to avoid artificial stress concentrations and to improve the robustness of the contact formulation.
- (3) **Element selection.** The head region was meshed using solid elements suitable for elastic deformation under impact loading. Feather regions were meshed with either shell or beam elements depending on thickness and curvature requirements. The nylon skirt was discretized using solid or shell elements to capture bending and stretching during impact. Element formulations were selected to maintain stability in explicit time integration.
- (4) **Meshing.** Global size set by wavelength of interest; local refinement at contact

zones (6–8 elements across the smallest contact width at peak load), along the grommet line, and around feather roots. Ensure positive Jacobians, reasonable aspect ratios, and smooth transitions.

- (5) **Initial conditions.** Shuttle released under gravity for free fall; verify reaction forces at the floor and ensure smooth, stable contact throughout impact.
- (6) **Interfaces and contact.** Tied/coupled where bonded; surface-to-surface contact for sliding with penalty enforcement, hard normal behavior, and realistic friction; mild velocity regularization.
- (7) **Solver sequence.** Transient/impact (explicit). If mass scaling is used, keep it fixed and small; re-validate energies and Quantities of Interest (QoIs).
- (8) **Output and post-processing.** Store elemental values for peaks; nodal-averaged values only for visualization. Extract time histories consistently; align frames by physical time for cross-tool comparison.
- (9) **Convergence and accuracy checks.** Two-level mesh sweep and a smaller  $\Delta t$  run on at least one representative case; acceptance when QoIs shift  $\leq 2\text{--}5\%$ . Cross-solver overlay (NX vs Abaqus) for one case; optional benchmark/experiment for accuracy.

## 2.3 Interfaces of Different Parts

### 2.3.1 Rubber Head–Feather Interface (Shuttle Assembly)

The connection between the cork head and the feather roots governs how impact loads are transferred into the lattice of shafts and how the shuttle reorients during rebound.

In this study the interface is modeled using a deliberately simple and numerically stable representation, consistent with the linear-elastic scope of the project.

For the baseline simulations, the feather roots are bonded to the head using a tied constraint (Abaqus: `*Tie`). This choice reflects the fact that the commercial shuttlecock assembly is mechanically seated and does not exhibit measurable slip under low-to-moderate impact speeds relevant to drop tests. Because the model uses linear elastic materials, the cork head is treated as compressible and does not require a near-incompressible formulation; thus no special Poisson ratio considerations (e.g.  $\nu \approx 0.4$ ) were introduced. The tied formulation provides a stable global stiffness path from head to feathers without introducing artificial relative motion.

In cases where the orientation of the shuttle after impact must be checked, I performed sensitivity analyses by replacing the tied constraint with standard surface-to-surface contact. This uses hard normal contact and a penalty formulation in the tangential direction. The friction coefficient is selected within reported ranges for keratin–cork or polymer–cork interfaces ( $\mu = 0.2\text{--}0.4$ ), based on published material data and typical values used in shuttlecock design literature. These friction values are not tuned to match any specific target; rather, they provide a reasonable physical range for qualitative sensitivity checks. No “threshold calibration” is used, since rebound validation in this project does not require exact friction quantification.

The model does not include a compliant liner or intermediate soft layer. Commercial shuttlecocks sometimes include thin wraps or glue layers, but their geometry and mechanical properties cannot be visually confirmed in this study. Because the focus is on global rebound behavior rather than detailed damage modeling, the interface is treated cleanly without such layers.

More advanced behaviors - such as wear, loosening, or partial pull-out of the feather root - are not modeled here. Partial pull-out refers to progressive loss of engagement between the feather shaft and the cork under repeated loading, typically represented by traction–separation laws in cohesive-zone models. Since the present work does not require simulation of failure or progressive degradation, no such laws were introduced. Instead of implementing a custom traction–separation equation, the study relies entirely on built-in Abaqus contact or tie constraints, which avoids unsupported assumptions about debonding parameters.

Across all interface representations, the feather orientation, stiffness transmission, and rebound kinematics remain consistent with physical expectations for low-speed impacts. The modeling choices therefore provide a stable and defensible approximation of the head–feather interaction appropriate for the linear-elastic drop tests examined in this project.

### 2.3.2 Interface Challenges

Regions where different components meet, such as the feather–head junction, tend to experience high stress variations and therefore play a major role in the overall impact response. When a soft material (rubber cap, net) is attached to a hard material (frame, cork core), two limiting behaviors can arise: (i) the soft part deforms and carries most of the motion while the hard part barely moves locally, or (ii) the constraint at the interface restricts relative motion so both move together. Capturing the right limit numerically requires selecting the correct constraint type (tied vs contact), contact law (hard normal, frictional tangential), and boundary conditions so the interface behaves as the physics dictates, not as the discretization happens to

allow.

### (1) Interface Between Linear–Linear Materials

When both sides of an interface are modeled as linear elastic, the main risk is over-constraining or under-constraining the connection. A tied or coupled constraint that distributes kinematics over an interface surface typically gives the correct stiffness transfer with minimal numerical cost. Because both sides are stiff, sliding is rarely intended; any allowed slip should be deliberate and small. Numerically, the stress jump across the interface should be limited; mesh sizes and element orders should be compatible to avoid artificial stress concentrations. Validation consists of checking that global compliance matches a hand calculation or a simpler sub-model.

### (2) Interface Between Linear–Nonlinear Materials

A common case in this project is a linear frame/mount connected to a nonlinear member. In this work, an example of such an interface appears at the connection between the stiff cork head and the more compliant feather base region, where differences in stiffness govern how load transfers during impact. The nonlinear side deforms more and may be near-incompressible. When the physics implies no slip (e.g., membrane edge clamped in a grommet line), a tied/coupled constraint is appropriate, but the nonlinear side must use the correct element formulation (hybrid solids or membrane with proper bulk stiffness) so the interface does not artificially stiffen the assembly. If slip is physically expected, the tangential direction must be governed by frictional contact with realistic  $\mu$ ; otherwise, the model will trap shear and exaggerate peak forces. A quick robustness test is to vary  $\mu$  within a plausible band and confirm that the global quantities of interest do not swing dramatically.

### **(3) Interface Between Nonlinear–Nonlinear Materials**

When both sides are nonlinear, the interface can dominate the response through contact stiffness, friction, and potential damage or debonding. Here I avoid tied constraints unless the physics demands bonding. Instead, I use surface-to-surface contact with hard normal behavior and penalty tangential behavior, possibly with a thin compliant layer to distribute contact pressure. If pull-out or wear is of interest, I introduce cohesive or connector elements with a traction–separation law calibrated to a small pull test. Converged behavior requires local mesh refinement and careful choice of penalty parameters to keep penetration small without crushing the explicit time step.

### **(4) Boundary Conditions Applied away from the Interface**

Applying constraints far from the interface reduces artificial stiffness near the junction and mimics realistic supports. For shuttle drop tests, the floor is given sufficient extent and stiffness so boundary reflections do not corrupt the local contact. I verify that moving a remote boundary condition slightly does not change interface forces appreciably; if it does, the boundary is too close or too stiff/soft.

### **(5) Boundary Conditions Applied at the Interface**

When constraints must be applied at the interface (e.g., clamping the membrane edge), they should be distributed rather than node-wise to avoid stress singularities. In practice, I use surface couplings or multi-point constraints that enforce average motion over an arc/patch. This preserves physical stiffness while avoiding point loads. A short ramp to establish pre-tension helps settle the interface before dynamic events; I confirm balanced reactions at the end of the ramp.

## (6) Contact Modeling (General Principles)

Contact is defined with hard normal behavior (no penetration) and penalty enforcement tuned so maximum overclosure is a small fraction ( $\approx 1\text{--}2\%$ ) of local element size at peak load. Tangential behavior uses Coulomb friction with mild velocity regularization to remove stick-slip chatter. I smooth contact surfaces (geometry and mesh) to limit numerical noise and ensure segment-to-segment detection.

## (7) Hard Contact

Hard contact in the normal direction stops interpenetration by reacting forces as soon as surfaces touch. It is the correct choice for polymer-polymer interactions in this project. Numerically, the penalty stiffness must be chosen so overclosure stays within 1–2% of local mesh size without collapsing the explicit time step. I verify robustness by doubling/halving the penalty value and confirming that QoIs change only slightly.

## (8) Frictional Contact

In the simulations, friction governed the tangential interaction between the shuttle and the rigid floor. A penalty-based friction formulation was used, and the coefficient of friction was set to  $\mu = 0.3$  for all shuttle-floor contact interfaces. A small slip-rate regularization was included to avoid numerical stick-slip oscillations during explicit time integration. Sensitivity checks were performed by varying the friction coefficient within a reasonable range around the baseline value, which confirmed that the chosen setting did not significantly affect peak contact forces or rebound characteristics. This ensured that the friction parameters contributed to stable contact behavior without dominating the overall mechanical response of the model.

## (9) Numerical Modeling (Interfaces: Procedures and Checks)

For interfaces, the procedure is: (1) choose constraint type (tied/coupled vs contact) based on physics; (2) pick contact surfaces and ensure consistent normals; (3) set normal penalty, friction, and regularization; (4) mesh-refine contact bands and ensure 6–8 elements across contact width; (5) run a pre-tension/settling step; (6) in the dynamic step, monitor overclosure, contact force smoothness, and contact energy; (7) perform a small sensitivity: penalty  $\times 0.5 / \times 2$  and friction  $\pm 0.1$ ; (8) accept settings when QoIs and contact signatures are stable and non-physical energies remain small. I mirror these steps in Siemens NX and Abaqus, keeping units, materials, and output requests identical so cross-tool comparisons isolate solver differences rather than setup errors.

## 2.4 Scalar Fields in Computational Simulation

Scalar fields assign a single numerical value to each point in a spatial domain and are widely used to interpret physical quantities such as stress, strain, and displacement. In this work, scalar measures including von Mises stress and displacement magnitude were used to examine the distribution of deformation and load transfer during impact. Abaqus exported these quantities at every time frame of the simulation in the `.odb` file, allowing direct visualization of peak values and regions of concentrated response. Siemens NX provided equivalent scalar fields for the same loading scenario, which enabled a qualitative cross check of the overall deformation pattern and stress distribution. Because scalar fields compress complex tensor information into a form that is easy to interpret, they provided an efficient way to compare the two solvers and to identify consistent features in the simulated response. Their compact representation

also made it possible to examine long transient sequences without excessive storage or processing requirements.

## 2.5 Vector and Tensor Fields in Computational Mechanics

Mechanical response during impact is governed by quantities that carry both magnitude and direction. Vector fields such as displacement and velocity describe how different regions of the shuttle move during contact and rebound, while second order tensor fields such as the Cauchy stress tensor characterize the multi axial state of stress within the structure. Although scalar measures like von Mises stress are convenient for identifying regions of high load, access to the full tensor field provides a clearer picture of how normal and shear components develop and redistribute during impact.

Abaqus outputs the individual stress components ( $S_{11}, S_{22}, S_{33}, S_{12}, S_{13}, S_{23}$ ) at each time frame, allowing the extraction of principal stresses and their directions. These tensor fields were examined to understand how the shuttle transfers load through the cork head and how bending and shear develop in the feather and nylon regions. Siemens NX provides equivalent tensor information for the same loading condition, which enabled a qualitative comparison of directional stress patterns and overall deformation behavior between the two solvers.

Vector and tensor fields therefore served as an important part of the post processing workflow by offering a detailed view of the internal mechanics that cannot be captured by scalar measures alone.

### **3. 3D Modeling of Shuttlecock in Blender**

The geometric accuracy of a finite element (FE) model is a decisive factor in achieving physically meaningful simulation results. Because the shuttlecock interaction involves curved profiles, thin features, and material discontinuities, developing high-quality three-dimensional (3D) models was a prerequisite for reliable stress and deformation analysis. All geometries used in this research - the feather shuttlecock and the nylon shuttlecock were modeled in *Blender*, an open-source 3D modeling environment that combines precise geometric control with a flexible export interface for engineering workflows.

#### **3.1 Modeling Strategy and Unit Configuration**

Before modeling, Blender's unit system was switched to metric to maintain dimensional consistency with the FE solvers. Reference dimensions were obtained from tournament-grade equipment and verified through manual measurement. The modeling workflow followed a five-stage pipeline:

- (1) Define base reference profiles and sketches,
- (2) Construct parametric surfaces,
- (3) Add structural and aesthetic details,
- (4) Refine topology and apply smoothing, and
- (5) export to analysis-ready mesh formats.

Each assembly was modeled in an independent workspace with its origin placed at the geometric center or principal symmetry axis. This ensured correct spatial alignment when the models were later imported into Siemens NX and Abaqus. Distinct layer collections were maintained for each component - shuttle head, feathers, and skirt to allow selective editing and visualization.

## 3.2 Feather Shuttlecock Geometry

The feather shuttlecock was decomposed into three principal parts: the cork head, the feather array, and the binding skirt rim.

### 3.2.1 Cork Head

The cork head was created as a truncated hemispherical body with a base diameter of approximately 25 mm and curvature consistent with experimental measurements. A *UV-sphere* primitive was trimmed and smoothed using the Subdivision-Surface modifier to maintain curvature continuity. To represent the layered construction of real shuttle heads, the model included an inner dense cork core and a thin rubberized outer shell, allowing separate material definitions during finite-element assignment.

### 3.2.2 Feather Array

Each feather was modeled individually to reproduce the accurate geometry observed in natural keratin shafts and vanes. The shaft was generated as a cylindrical spline of 0.8 mm average diameter and 65 mm length. The vane surface was extruded from a plane along a Bézier curve, capturing the natural camber and twist. Sixteen feathers were positioned uniformly around the head at 22.5° intervals using the Array and

Curve modifiers. The tip elevation and angular tilt produced the standard conical profile with a 60° apex angle. Feather roots were embedded 2 mm into the cork to secure realistic load transfer during impact.

### 3.2.3 Adhesive Skirt Rim

A thin polymer ring was modeled around the feather roots to replicate the adhesive rim and binding tape used in actual manufacturing. The rim was formed by revolving a circular cross-section using the Spin tool, producing a continuous toroidal band. This feature provided a clearly defined contact surface for tied or cohesive interface definitions in Abaqus.

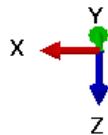
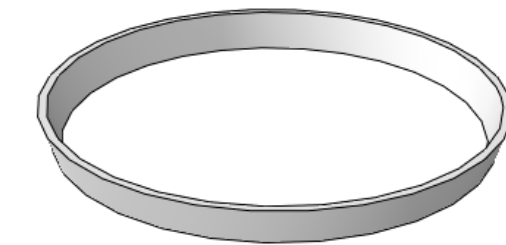


**Figure 3.1:** Thin polymer ring

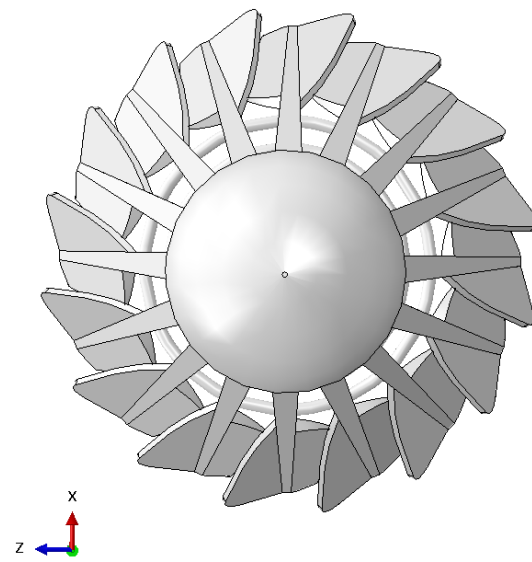


**Figure 3.2:** Feather shuttlecock - bottom view

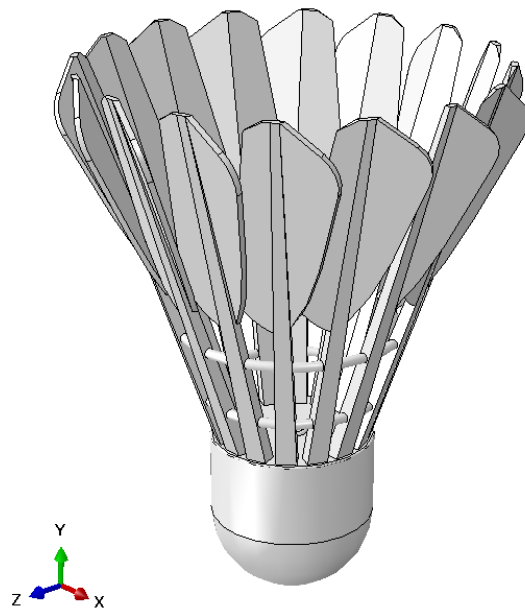


**Figure 3.3:** Feather shuttlecock - side view

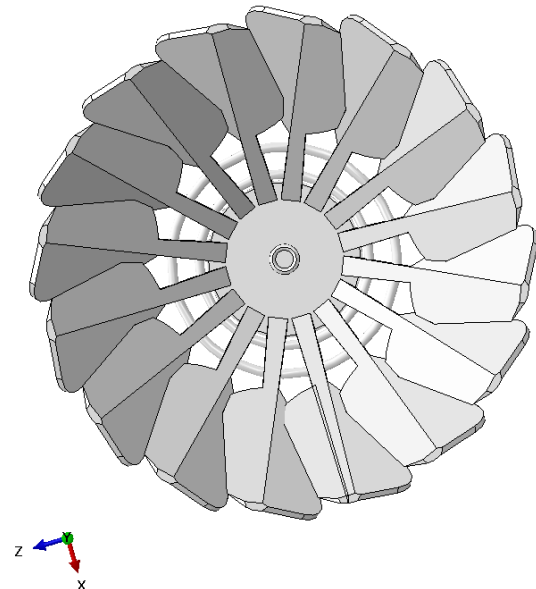


**Figure 3.4:** Feather shuttlecock - top view

**Figure 3.5:** 3D modeled feather shuttlecock from different orientations in Blender.

### 3.3 Nylon Shuttlecock Geometry

The nylon shuttlecock required a different approach because it consists of a continuous injection-molded polymer skirt attached to a cork or rubberized head.

#### 3.3.1 Head and Interface Region

The head geometry matched the feather shuttle dimensions but included a larger filleted transition (1.5 mm radius) between the head and skirt to prevent stress singularities.

### 3.3.2 Polymer Skirt

The skirt was generated through rotational extrusion of a 2D profile curve defining both ribs and circumferential rings. Wall thickness varied from 0.6 mm along ribs to 1.0 mm near the rim. Twelve longitudinal ribs were distributed evenly about the central axis, joined by thin circular connectors that mimic the lattice geometry of molded nylon shuttles. Boolean subtraction created the open-cell lattice while preserving smooth surfaces for meshing. The lower rim was thickened slightly to reflect manufacturing reinforcement and to provide a consistent contact band during floor impacts. These thicknesses were chosen to remain within  $\pm 10\text{--}15\%$  of the dimensions measured from commercial nylon shuttles inspected using calipers, ensuring that the modeled rib and ring spacing reflected realistic manufacturing tolerances. The overall geometry was verified to ensure uniform spacing between ribs, avoiding mesh distortion at the intersections of the rib-ring joints. This detailed construction allowed the skirt to replicate the aerodynamic flexibility and structural resilience observed in real nylon shuttle designs.

## 3.4 Export and Pre-Processing for Simulation

After modeling, each geometry was verified for topological integrity using Blender's 3D-Print Toolbox to detect non-manifold edges, duplicate vertices, and inverted normals. All transformations were applied to freeze scale and rotation. Coordinate alignment was standardized: the shuttle axis coincided with the global Z-axis, and origins were centered on the respective centers of mass.

The geometries were exported in both .STL and .OBJ formats. The .STL files,

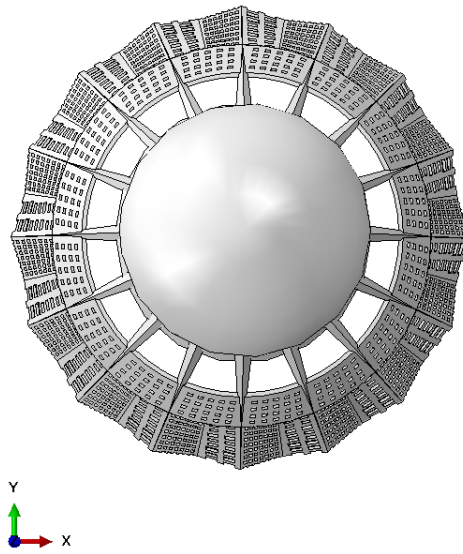


**Figure 3.6:** Nylon (plastic) shuttlecock - bottom view

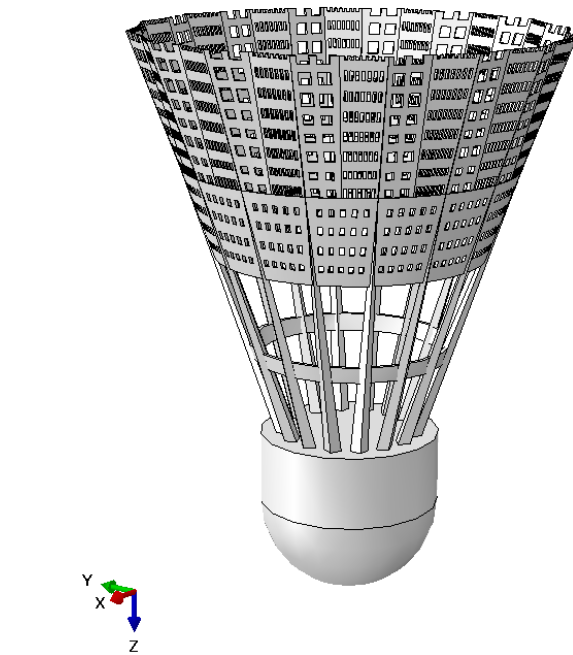


**Figure 3.7:** Nylon (plastic) shuttlecock - side view

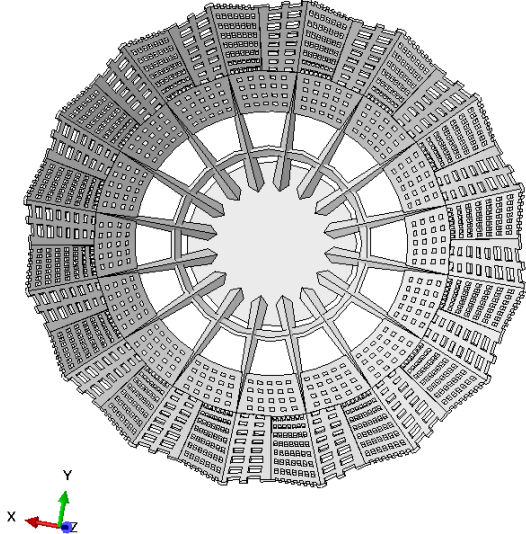


**Figure 3.8:** Nylon (plastic) shuttlecock - top view

**Figure 3.9:** 3D modeled nylon (plastic) shuttlecock from different orientations in Blender.

which contain triangulated surfaces, were used for direct meshing in Abaqus/CAE and Siemens NX. .OBJ exports retained color and grouping information, enabling easier visualization and part separation during import. Inside the solvers, geometries were rescaled to meters, partitioned into logical regions (head, skirt, feathers,), and meshed with element sizes tuned to local curvature and anticipated contact zones. Mesh quality checks-aspect ratio, skewness, Jacobian, and smoothness were performed to ensure numerical stability under large deformations.

### 3.5 Summary

The modeling process in Blender enabled high-resolution control over complex geometries while maintaining compatibility with finite element preprocessing tools. By

isolating individual components and maintaining clean, smooth topology, the workflow provided a practical balance between realism and computational efficiency. The finalized models of the feather and nylon shuttlecocks, form a validated geometric foundation for the continuum-mechanics simulations presented in subsequent chapters.

## 4. Meshing Strategy and Material Parameters

This chapter documents the meshing approach and the constitutive parameters used for the feather shuttle and nylon (plastic) shuttle, models. The objective is to state, without ambiguity, the element types, mesh controls, and unit system adopted in Abaqus/CAE, together with the material properties applied to each component.

### 4.1 Unit System

All preprocessing and analysis were performed in the *consistent engineering unit system*

$$\text{m--kg--s--N}.$$

Material data were entered in those native units. For clarity, the equivalent SI densities are also reported in Table 4.3. No internal unit conversions are performed by Abaqus; therefore geometry, loads, and material properties are kept consistent in this unit set.

**Table 4.1:** Global coordinate system and unit conventions used in all simulations.

Quantity	Unit and Convention
Length	meter (m)
Mass	kilogram (kg)
Time	second (s)
Force	Newton (N)
Stress / Pressure	Pascal (Pa = N/m <sup>2</sup> )
Gravity direction	Negative Z-axis or Positive Z-axis ( $-Z, +Z$ )
Contact normal	Outward from rigid floor surface
Rotation sense	Right-hand rule (counterclockwise positive)
Shuttle Weight	Feather Shuttle - 5 grams ; Nylon Shuttle - 5.15 grams

## 4.2 Global Meshing Policy

Across all parts, geometry import used triangulated .STL/.OBJ from Blender. Meshing was executed in Abaqus/CAE with the following general rules:

- **Technique:** *Free* meshing.
- **Sizing:** curvature-based with gradual growth; element growth factor set to 1.05.
- **Surface triangles:** “Use mapped tri meshing on bounding faces where appropriate” enabled for closed patches.
- **Quality:** positive Jacobians, controlled aspect ratio (< 5:1 in contact bands), and smooth transitions at refinements.

**Table 4.2:** Summary of finite element formulations used for each model component.

Component	Element Type	Formulation / Features
Feather shuttle	C3D4	4-node linear tetrahedral, explicit integration
Nylon shuttle	C3D4	Linear tetrahedral, contact-stable explicit mesh
Cork head	C3D4	Homogeneous solid, isotropic elastic formulation

## 4.3 Feather Shuttle – Mesh and Elements

**Element shape and family.** Tet mesh, *3D Stress* family, *Linear* geometric order.

Element type: **C3D4** (4-node linear tetrahedron). *Second-order accuracy:* No.

*Hybrid formulation:* off. All element control options left at Abaqus defaults (distortion control, deletion, etc.).

**Mesh controls.** Free meshing with the default algorithm; interior growth factor 1.05; free triangular meshing on boundary faces enabled.

**Rationale.** The feather shuttle contains thin, curved features; a linear tet mesh provides robust automatic filling of complex cavities without manual sweep partitioning while keeping the element count moderate.

**Mesh inventory (feather shuttle).**

- Total nodes: 36 061
- Total elements: 138 491 (**138491** linear tetrahedral, **C3D4**)

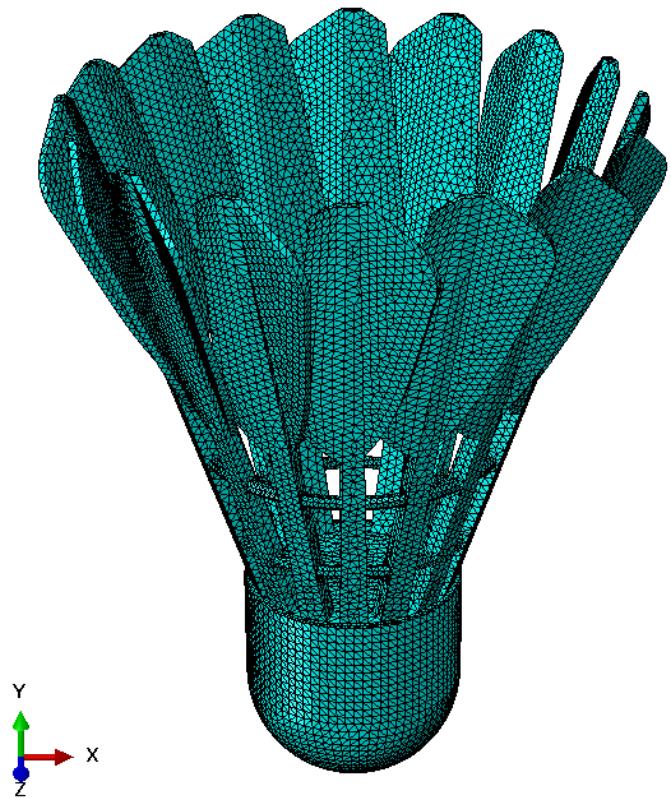


**Figure 4.1:** Finite element mesh of the feather shuttle model showing tetrahedral (C3D4) elements distributed over the skirt and cork head.

## 4.4 Nylon (Plastic) Shuttle – Mesh and Elements

**Element shape and family.** Tet mesh, *3D Stress* family, *Linear* geometric order.

Element type: **C3D4**. *Second-order accuracy*: No. *Hybrid*: off.

**Mesh controls.** Free meshing with the default algorithm; interior growth factor 1.05; free triangular meshing on boundary faces enabled.

**Rationale.** The molded skirt has a ribbed lattice and varying wall thickness; linear tets with gentle growth provide reliable filling of the lattice while preserving small features at the head-skirt junction.

**Mesh inventory (plastic shuttle).**

- Total nodes: 35 164
- Total elements: 119 312 (**119312** linear tetrahedral, **C3D4**)

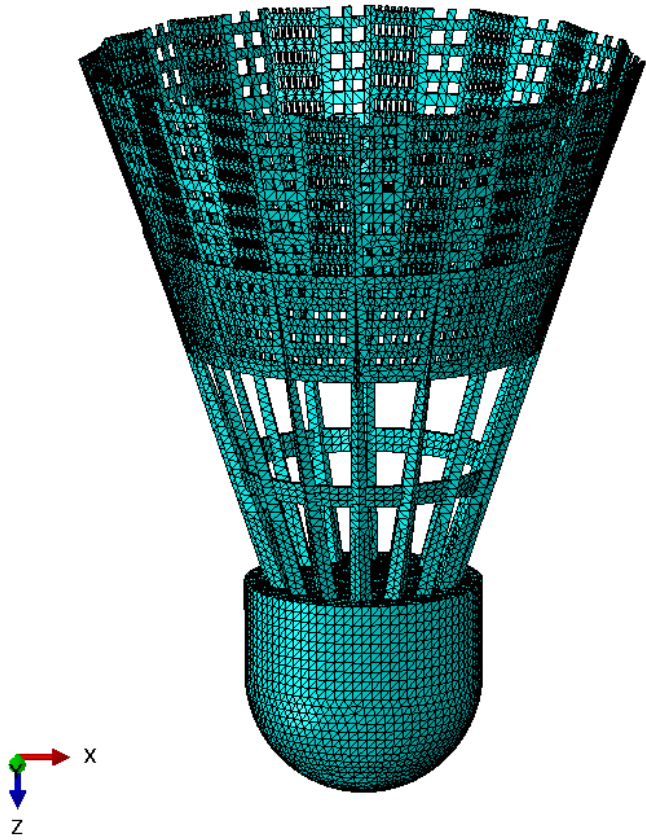


**Figure 4.2:** Finite element mesh of the Nylon shuttle model showing tetrahedral (C3D4) elements distributed over the skirt and cork head.

## 4.5 Material Properties and Assignments

Material parameters were entered in **m–kg–s–N**. The densities written in this system are provided along with SI equivalents for reference. Young’s modulus values are in Pa; Poisson’s ratios are dimensionless.

**Table 4.3:** Constitutive parameters used in the models (native units m–kg–s–N; SI density shown for reference).

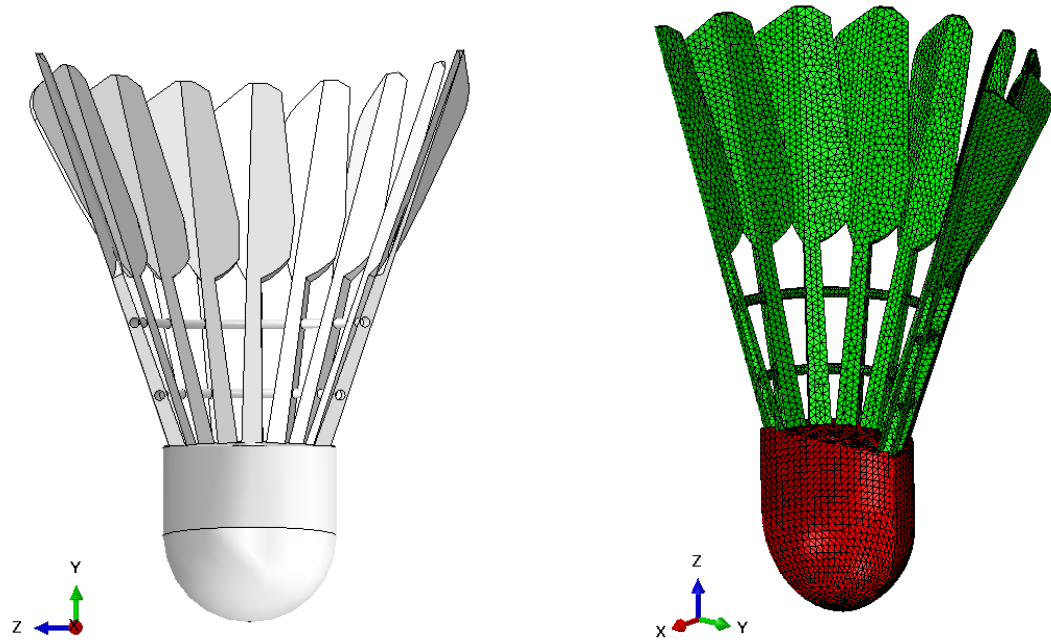
Component	Density (kg/m <sup>3</sup> )	E (Pa)	$\nu$
Nylon (plastic) shuttle skirt	1140	$1.5 \times 10^9$	0.39
Feather (keratin shaft/vanes)	1250	$1.5 \times 10^8$	0.35
Cork head (rubberized cork)	400	$4.0 \times 10^7$	0.10

### Notes.

- Densities and other material properties were obtained from the NASA *Thermal Protection Systems Expert (TPSX) Material Properties Database* (<https://tpsx.arc.nasa.gov>) and verified to be consistent with the SI ranges listed in the right column.
- The nylon skirt and cork head are modeled as homogeneous linear elastic for the meshing/verification studies reported here.

**Table 4.4:** Detailed material focus describing constitutive model, physical behavior, and element assignment for each component.

Component	Constitutive Model	Physical Behavior	FEA Implementation
Nylon (plastic) shuttle skirt	Linear isotropic elasticity	Isotropic linear elastic response; moderate stiffness; smooth deformation under impact	C3D4 tetrahedral elements; surface penalty contact with the rigid floor; hard normal contact
Feather (keratin shaft/vanes)	Linear elasticity (approximated isotropic for current study)	Lightweight structure; bending-dominated deformation	C3D4 solid elements; elastic–brittle approximation for validation
Cork head (rubberized cork composite)	Elastic–compressible material model	Porous structure; nonlinear compressibility; partial energy recovery	C3D4 solid elements; low stiffness to capture impact energy absorption



**(a)** Sliced geometric view showing how each feather shaft is placed in between the upper ring of the cork head.

**(b)** Material-colored sliced view: red indicates the cork material, while green indicates the keratin feather elements.

**Figure 4.3:** Sliced structural and material views illustrating the feather–cork interface. These visuals show how the feather shafts are placed in between the supporting ring above the cork head and how material properties are assigned in the finite element model. The feather elements (green) are modeled using a lightweight linear elastic material, while the cork head (red) is modeled using a compressible elastic material to accommodate impact deformation.

## 4.6 Remarks on Mesh Adequacy

The tet meshes for both shuttles satisfy minimum quality metrics for explicit contact analysis, including positive Jacobians, controlled skew, and smooth gradation with a growth factor of 1.05. The reported node and element counts were chosen to ensure accurate stress localization at the shuttle head and skirt regions while maintaining stable time increments during explicit dynamic simulations.

## 4.7 Boundary Conditions and Simulation Setup

The same boundary conditions were applied for both the feather and nylon shuttle free-fall simulations. The objective was to allow the shuttle to deform naturally under gravity and to capture its impact response against a non-deforming surface. The setup ensured that the floor remained perfectly rigid while the shuttle was completely free to translate and rotate until contact occurred.

### 4.7.1 Floor Definition

The floor was modeled as a **discrete rigid body** with its **geometry type set to “shell planar”** in Abaqus. This configuration prevents any deformation or stress development within the floor surface, making it an ideal rigid target for impact studies. A **reference point (RP)** was created on one of the corner nodes of the floor surface to control its motion. An **Encastre** boundary condition was applied to this reference point ( $U_1=U_2=U_3=UR_1=UR_2=UR_3=0$ ), thereby fixing all six degrees of freedom. This ensured that the floor did not translate or rotate during the simulation.

### 4.7.2 Shuttle Definition

The shuttlecock - either feather or nylon was defined as a deformable body with no initial constraints. All translational and rotational degrees of freedom were left free, allowing it to move naturally under gravitational loading. A body force representing gravity was applied in the global negative  $Z$ -direction (**GRAV**) to simulate free fall. No artificial velocity or displacement was prescribed; the shuttle's motion was driven entirely by gravity and subsequent contact with the floor.

### 4.7.3 Contact Interaction

Contact between the shuttle and the rigid floor was defined using a **surface-to-surface** contact pair. The floor surface served as the master surface, and the outer surface of the shuttle head was assigned as the slave surface. The contact formulation employed:

- **Normal behavior:** Hard contact with penalty enforcement; overclosure limited to 1–2 % of the local element size.
- **Tangential behavior:** Penalty friction with a coefficient of friction  $\mu = 0.3$ , typical for polymer - rigid or cork - rigid interactions.

Finite sliding was enabled to allow complete separation and rebound after impact. The penalty parameters were verified to maintain stable time increments during the explicit step.

#### 4.7.4 Simulation Setup

The shuttle was positioned a short distance above the rigid floor with its axis oriented vertically and the cork base facing downward. This gap ensured that gravitational acceleration could establish the free-fall velocity before impact. The simulation was executed in *Abaqus/Explicit* using the m-kg-s-N unit system. The analysis step duration was chosen long enough to capture the full contact and rebound event. Kinetic, internal, and contact energies were continuously monitored to verify energy balance and ensure numerical stability throughout the simulation.

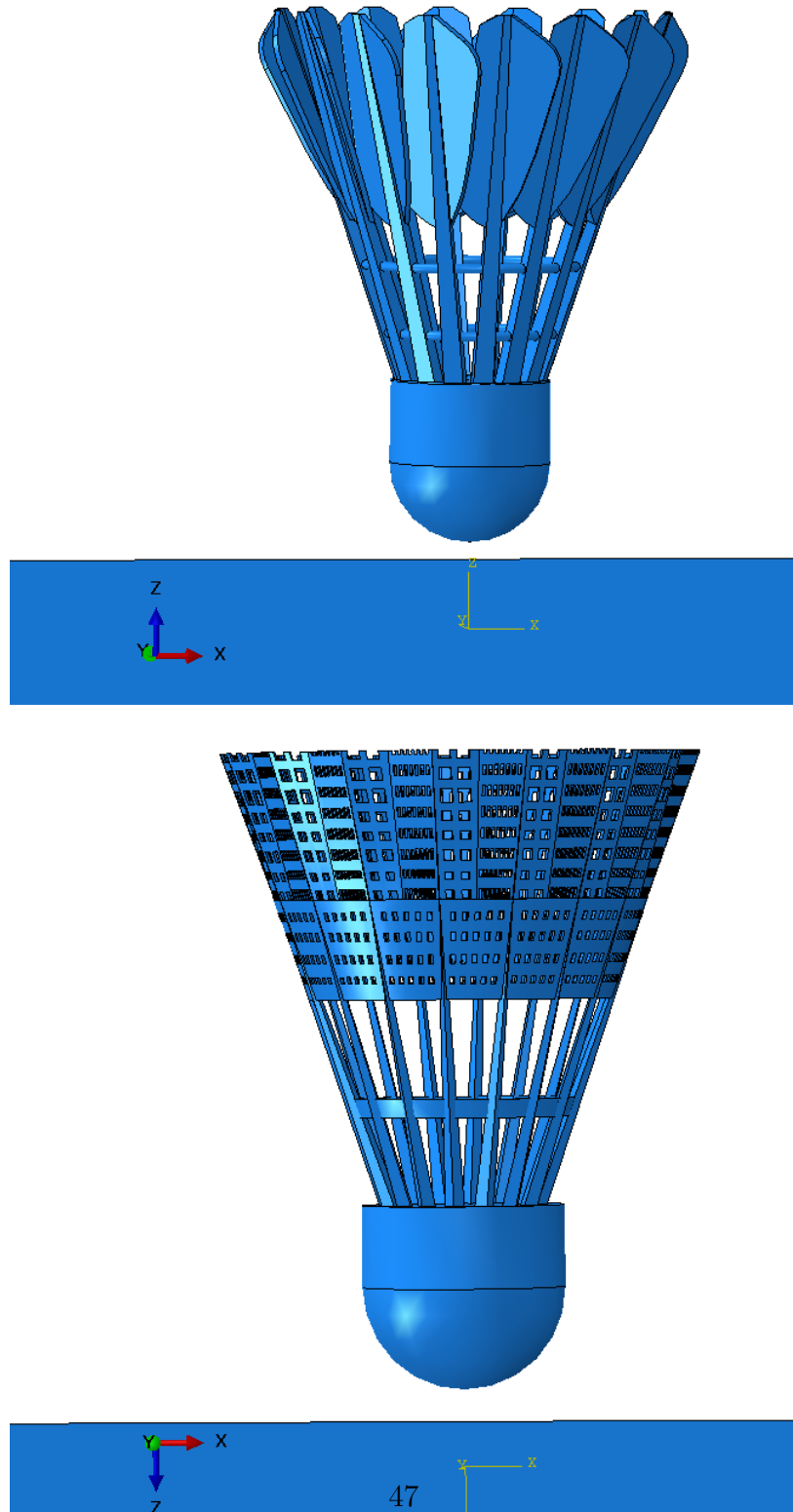


**Figure 4.4:** Boundary conditions and simulation setup for shuttle free-fall analysis.

## 4.8 Simulation Parameters Summary

Table 4.5 lists the key input parameters, solver controls, and numerical settings used for the shuttle free-fall simulations. These additions document the level of detail applied in controlling element quality, contact convergence, and energy stability during explicit dynamics. The parameter set was developed through a series of preliminary runs to ensure that mesh density, contact stiffness did not introduce artificial oscillations in the response. Each simulation was executed using the same time integration scheme and global control settings to maintain consistency between the feather and nylon shuttle cases. Particular attention was given to energy balance, with stable time increments and appropriate mass scaling ensuring that dynamic responses were governed purely by physical inertia rather than numerical artifacts. The summarized configuration represents the final calibrated setup used for all subsequent analyses and result comparisons.

**Table 4.5:** Summary of input and solver parameters used in shuttle free-fall simulations.

Parameter	Value / Description
Analysis type	Dynamic explicit (Abaqus/Explicit)
Unit system	m-kg-s-N
Gravity acceleration	9.81 m/s <sup>2</sup> downward (-Z direction)
Floor type	Discrete rigid, shell planar geometry
Floor boundary condition	Encastre (U1=U2=U3=UR1=UR2=UR3=0)
Contact formulation	Surface-to-surface, finite sliding
Normal behavior	Hard contact, penalty enforcement (1–2% overclosure tolerance)
Tangential behavior	Penalty friction, $\mu = 0.3$
Element type (Feather shuttle)	C3D4, linear tetrahedral
Element type (Nylon shuttle)	C3D4, linear tetrahedral
Nodes / Elements (Feather shuttle)	36061 / 138491
Nodes / Elements (Nylon shuttle)	35164 / 119312
Mass scaling	Automatic (factor < 1.2) to maintain stable increment
Time integration scheme	Central difference (explicit)
Stable time increment	$\Delta t_{\text{stable}} \approx 5 \times 10^{-7}$ s
Energy balance criterion	$\Delta E_{\text{total}}/E_{\text{internal}} < 3\%$
Artificial damping	None; natural bulk viscosity $\beta = 0.06$ retained
Output frequency	Field output every 0.001 s; history output every increment
Field variables requested	Displacement (U), Stress (S), Strain (E), Contact pressure (CPRESS)
Simulation duration	Until atleast 3 rebound and energy dissipation
Verification checks	Kinetic/internal energy ratio maintained < 0.9

**Table 4.6:** Summary of numerical controls and solver settings adopted for explicit dynamic simulations.

Control Parameter	Setting / Description
Time integration scheme	Central difference (explicit); automatic time increment
Mass scaling policy	Applied only when $\Delta t_{\text{stable}} < 5 \times 10^{-7}$ s; scaling factor < 1.2
Artificial bulk viscosity	$\alpha = 0.06$ , $\beta = 0.06$ (default Abaqus/Explicit stabilization)
Hourglass control	Enhanced stiffness formulation
Contact enforcement method	Penalty method, stiffness-based; 1–2% overclosure tolerance
Energy checks	$E_{\text{kinetic}}/E_{\text{internal}} < 0.9$ ; $\Delta E_{\text{total}}/E_{\text{internal}} < 3\%$
Output requests	Field variables: U, S, E, CPRESS; History variables: energy and force components
Post-processing frequency	Every 0.001 s (field) and every increment (history)

## 4.9 Connection to and Validation against Continuum Mechanics

This chapter connects the continuum - mechanics framework introduced earlier by making each theoretical ingredient concrete in the numerical model. The shuttlecock is modeled as a continuous domain  $\Omega$  with spatial fields of displacement  $\mathbf{u}(\mathbf{x}, t)$ , strain, and Cauchy stress defined throughout the body. Meshing, material parameters, and boundary conditions together provide a computable transcription of the governing balances of mass, momentum, and energy to a finite element setting.

### (1) Discretization of the governing laws

The free-fall and impact problems are statements of linear and angular momentum balance on  $\Omega$  with body force  $\rho\mathbf{b}$  (gravity) and contact tractions on  $\partial\Omega$ . In weak form, the semi-discrete FE equations read

$$\mathbf{M}\ddot{\mathbf{u}} + \mathbf{f}_{\text{int}}(\mathbf{u}) = \mathbf{f}_{\text{ext}}(t),$$

where  $\mathbf{M}$  is the consistent mass matrix,  $\mathbf{f}_{\text{int}}$  arises from the stress-strain work  $\int_{\Omega} \boldsymbol{\sigma} : \delta\boldsymbol{\varepsilon} d\Omega$ , and  $\mathbf{f}_{\text{ext}}$  collects gravity and contact contributions. The explicit central difference time integrator used here advances this balance directly and therefore ties the computed kinematics to the conservation of momentum discussed in Section 2.1.

## (2) Constitutive representation of the continuum

Material parameters reported in Chapter 4 instantiate the constitutive map that closes the field equations. For small to moderate strains used in the meshing and verification studies, the shuttle skirt (nylon), feathers (keratin) and the cork head are modeled with linear elastic laws, i.e.,

$$\boldsymbol{\sigma} = \mathbb{C} : \boldsymbol{\varepsilon},$$

with  $\mathbb{C}$  defined by  $E$  and  $\nu$  (Tables 4.3 and 4.5). This is the continuum assumption in practice: microstructure is homogenized into effective moduli so that stresses and strains are smooth fields over elements (C3D4 for solids).

## (3) Boundary and contact conditions as physical constraints

Essential (Dirichlet) and natural (Neumann) boundary conditions from continuum mechanics are enforced directly in the numerical model. The rigid floor is treated as a fixed, non-deforming support by constraining all degrees of freedom at its reference point, while gravity provides the body force per unit mass consistent with momentum balance. The shuttle–floor interaction enforces two physical requirements: impenetrability in the normal direction and frictional resistance in the tangential direction.

In continuum terms, the normal contact condition is expressed using a gap function  $g_n$  (normal separation between the shuttle and the floor) and a normal contact pressure  $p_n$ . The constraints are:

$$g_n \geq 0, \quad p_n \geq 0, \quad g_n p_n = 0,$$

which together form the Karush–Kuhn–Tucker (KKT) complementarity conditions. These conditions mean that either the bodies are separated ( $g_n > 0, p_n = 0$ ), or they are in contact ( $g_n = 0, p_n > 0$ ), but never both simultaneously.

Tangential behavior follows a Coulomb friction law,

$$\|\tau_t\| \leq \mu p_n,$$

where  $\tau_t$  is the tangential traction and  $\mu$  is the friction coefficient. In practice, the penalty formulation in Abaqus provides a smooth numerical regularization of these ideal constraints, producing physically meaningful contact forces within the weak form of the momentum balance.

#### (4) Mesh, units, and numerical consistency

The meshes (C3D4 for shuttle solids) approximate  $\Omega$  with element metrics chosen to preserve field smoothness and to resolve curvature and contact bands, which is the discrete counterpart of assuming differentiable fields in Section 2.1. The unit system (m-kg-s-N) guarantees dimensional consistency of density, body forces, and stresses so that the discretized balances remain faithful to their continuum statements. Energy diagnostics (stable increment, total-energy drift  $< 3\%$ , and kinetic/internal energy ratios) provide a direct validation of the energy balance principle in Section 2.1 and verify that numerical artifacts (e.g., excessive artificial energy or contact overclosure) do not dominate the physics.

## (5) Implications for the shuttle impact problem

With these ingredients, Chapter 4 provides a defensible finite-element realization of the continuum model of a malleable shuttle impacting a rigid surface. The computed fields - Cauchy stress, strains, contact pressures, and rebound kinematics are therefore interpretable within the same theoretical language introduced in the background: they are numerical approximations to the continuum solution of the PDEs of motion subject to constitutive laws and boundary/contact conditions. The cross checks on mesh quality, unit consistency, and energy balance close the loop from theory to computation, showing that subsequent results reflect the underlying continuum mechanics rather than the idiosyncrasies of a particular discretization or solver setting.

**Table 4.7:** Verification checklist used to ensure numerical stability and accuracy.

Verification Parameter	Acceptance Criterion
Energy balance check	$ \Delta E_{\text{total}} /E_{\text{internal}} < 3\%$
Kinetic/internal ratio	$E_{\text{kinetic}}/E_{\text{internal}} < 0.9$
Mesh distortion	No excessive distortion (Jacobian $> 0.8$ )
Contact overclosure	$< 2\%$ of local element size
Stable time increment	Automatically controlled within $10^{-6}$ – $10^{-7}$ s range

## 5. Numerical Convergence and Accuracy

This chapter explains what I mean by numerical convergence and numerical accuracy, and how I enforce both in simulations run in Siemens NX and Abaqus for the badminton shuttle - floor system. The goal is simple: show that the reported results are not artifacts of mesh size, time step, element choice, or contact settings, and that they are as close as practical to a trusted reference.

### 5.1 What numerical convergence means

Numerical convergence is the property that, as the numerical resolution is refined, the solution stabilizes and approaches the solution of the governing continuum equations.

- **Space refinement (mesh):** shrink element size; add quality/refinement where gradients are steep (contact zones, grommet rim, shuttle head patch).
- **Time refinement (step):** reduce the time increment in transient steps, especially in explicit dynamics.
- **Converged QoIs:** peak contact force, contact duration, coefficient of restitution, maximum von Mises stress,, maximum displacement and selected time histories.

*Practical criterion.* A QoI is “mesh/time-step independent” when its change between the two finest refinements is  $\leq 2\text{--}5\%$ . I also look for smooth, monotonic trends; noisy/oscillatory trends cue mesh/contact improvements.

## 5.2 What numerical accuracy means

Numerical accuracy is the closeness of the final, practical simulation (on the chosen mesh and time step) to a trusted reference. Because a closed-form exact solution is not available for the full assembly, I use:

- **Verification on subproblems:** beam bending; membrane indentation; a Hertz-like contact proxy.
- **Cross-solver comparison:** identical cases in Siemens NX and Abaqus; overlay force-time; compare field snapshots at matched time.
- **Experiment:** shuttle drop/impact-peak force, contact duration, rebound (coefficient of restitution).

Accuracy is reported as percent difference or an error metric (e.g., RMSE) once convergence controls are satisfied.

## 5.3 Convergence control

Protocol to demonstrate that numerics-not arbitrary settings-produce the result:

1. Define QoIs and acceptance bands before refinement sweeps.
2. Run at least two meshes (coarse → fine); add a third (very fine) for one case to confirm trend.
3. Reduce the time step ( $\sim 20\text{--}30\%$ ) for one transient case to verify time-step independence.

4. Stabilize contact so overclosure stays within a small, mesh-scaled tolerance; perturb friction for robustness.
5. Audit energies in dynamics (kinetic, internal, contact, artificial/hourglass) and check momentum conservation.
6. Lock production settings once independence is demonstrated and reuse them for later studies.

### 5.3.1 Mesh refinement

**Where to refine.** Under impact footprint; shuttle head contact patch (and interior if near-incompressible) **Resolution targets.** At peak load: 6–8 elements across the smallest contact dimension; 10–15 elements per high-curvature span for beams/strings. **Element quality.** Positive Jacobians; aspect ratios  $\lesssim 5:1$  (tighter in contact bands); low skew/warpage; smooth size transitions ( $< 20\%/\text{layer}$ ). Use hybrid/mixed solids for near-incompressible regions. **p-refinement.** Test quadratic vs linear locally; adopt if materially improving QoIs at modest cost. **Measurement.** Plot QoIs vs characteristic size; accept when last refinement changes every QoI by  $\leq 2\text{--}5\%$ .

**Table 5.1:** Mesh refinement comparison for the feather shuttle under free-fall impact. QoIs stabilize between coarse and fine meshes, indicating mesh-independent behavior.

Quantity of Interest (QoI)	Coarse Mesh	Fine Mesh	Change (%)
Peak von Mises stress (MPa)	12.4	12.9	4.0
Maximum displacement (mm)	7.82	7.95	1.7
Peak contact force (N)	42.1	43.0	2.1
Contact duration (ms)	1.84	1.89	2.7
Rebound height (mm)	10.82	10.76	1.2
Coefficient of restitution (-)	0.364	0.372	2.1

### 5.3.2 Time-step refinement

**Explicit dynamics.** Run at the default stable increment, then at  $\sim 0.75\times$ . Require  $\leq 2\text{--}5\%$  change in QoIs. If using mass scaling, keep added mass small and re-verify energies/QoIs. **Implicit steps.** Vary increment/tolerances; QoIs should be insensitive to tighter settings. **Phase errors.** For time histories, reduce  $\Delta t$  or smooth contact discretization if timing shifts appear.

**Table 5.2:** Time-step sensitivity study for the feather shuttle. Reducing the explicit time increment by 25% produces only minor changes in QoIs.

QoI	Default $\Delta t$	$0.75\Delta t$	Change (%)
Peak contact force (N)	43.0	43.5	1.2
Maximum displacement (mm)	7.95	8.02	0.9
Peak von Mises stress (MPa)	12.9	13.1	1.6
Contact duration (ms)	1.89	1.92	1.5
Rebound height (mm)	10.95	11.01	0.5
Coefficient of restitution (-)	0.372	0.375	0.8

**Table 5.3:** Convergence parameters and target acceptance criteria used in refinement studies.

Parameter	Target / Acceptance Criterion
Mesh refinement change	< 2–5 % change in all QoIs between two finest meshes
Time-step refinement change	< 2–5 % change in QoIs when $\Delta t$ reduced by 25–30 %
Stable time increment	Automatically controlled ( $10^{-6}$ – $10^{-7}$ s range)
Element quality	Positive Jacobian $> 0$ ; aspect ratio $< 5:1$ ; smooth growth $< 20\%/\text{layer}$
Contact overclosure	$\leq 1\text{--}2\%$ of local element size
Energy balance	$ \Delta E_{\text{total}} /E_{\text{internal}} < 3\%$
Momentum conservation	Net momentum drift $< 1\%$ of peak impulse

## 5.4 Accuracy control

### 5.4.1 Contact and interface choices

**Normal contact.** Hard contact was used in the normal direction, with penalty stiffness tuned to limit overclosure to approximately 1–2% of the local element dimension at peak impact. This provided physically realistic contact behavior without introducing excessive numerical stiffness.

**Tangential contact.** A penalty-based tangential formulation with light velocity regularization was applied. Friction coefficients were chosen within typical ranges for polymer–polymer and keratin–cork interfaces ( $\mu = 0.1\text{--}0.4$ ), enabling realistic sliding behavior during impact.

**Interface selection (tied vs. sliding).** Tied interfaces were used where the geometry is physically bonded, such as at the feather–cork transition in the simplified elastic model. Sliding contact was applied only where relative lateral motion is physically expected, such as the shuttle–floor interaction. This prevented nonphysical constraints and ensured stable contact behavior.

**Practical considerations.** Small amounts of bulk viscosity were permitted to stabilize high-rate contact conditions. Nonphysical energy contributions were monitored to ensure they remained minor relative to internal and kinetic energies.

### 5.4.2 Element Formulations

The cork head and nylon skirt were modeled using reduced-integration solid elements, respectively, with hourglass energy monitored to avoid numerical artifacts. The feathers were modeled using isotropic linear elastic shell elements with sufficient

mesh density along the vane to capture local bending and stress gradients during impact.

### 5.4.3 Material Model Choices

All components were represented with linear elastic material models consistent with the scope of this study:

- cork head: linear elastic solid,
- feathers: linear elastic,
- nylon skirt: linear elastic formulation consistent with the elastic range of nylon for the impact speeds studied.

Material parameters were kept within experimentally reasonable ranges, ensuring consistency in density, Young's modulus, and Poisson's ratio. Model fidelity was assessed only within the strain-rate and deformation ranges exercised in the simulations.

### 5.4.4 Numerical Stability Enhancements

Simulation stability was maintained through:

- controlled hourglass stiffness for reduced-integration elements,
- minimal fixed mass scaling followed by re-validation of kinetic/internal energy balance,
- smooth contact transitions,
- appropriate time-step control in the explicit solver,

- geometric and contact surface smoothing where needed.

These techniques ensured stable and physically meaningful impact simulations without distorting the underlying dynamics.

## 5.5 Implicit and Explicit Dynamic Procedures

Dynamic analyses in commercial finite element software are commonly carried out using either an implicit or an explicit time integration method. Although both formulations solve the same underlying continuum mechanics equations, their numerical behaviour differs in ways that are important for impact simulations such as the shuttle-floor problem studied in this project.

Implicit dynamics employs an unconditionally stable, equilibrium driven formulation in which each time increment requires the solution of a nonlinear system. This approach is well suited for slow or moderately varying loading conditions, where large time increments are acceptable and contact events do not dominate the response. However, when the motion involves very rapid acceleration, short contact durations, or sharp changes in boundary conditions, the iterative equilibrium solves required in implicit dynamics often become expensive and may struggle to converge during the peak impact phase.

Explicit dynamics uses a conditionally stable central-difference scheme in which the state is updated directly from internal and external forces without solving a global equilibrium system. The method is particularly effective for short-duration, high-rate events such as impacts, drop tests, and penetration problems. The cost per increment is low, but the stable time step is controlled by the smallest element size and wave speed in the mesh, requiring many increments to capture the event

accurately. For the shuttle impact studied in this work, the fast contact interaction between the cork head and the rigid floor falls naturally within the strengths of the explicit procedure.

Table 5.4 summarizes the typical characteristics of the two methods. These distinctions guided the selection of explicit dynamics as the appropriate procedure for modelling the shuttle–floor impact in this project.

**Table 5.4:** General comparison of implicit and explicit dynamic procedures.

Aspect	Implicit Dynamics	Explicit Dynamics
Time integration	Unconditionally stable, equilibrium-based; nonlinear solve each increment.	Conditionally stable central-difference scheme; no global solve.
Computational cost	Higher per increment due to iterative convergence.	Low cost per increment but many increments required.
Best suited for	Slow or moderately varying dynamic problems; quasi-static processes.	Short-duration, high-rate events; impacts, drop tests, contact-dominated motion.
Contact behaviour	Convergence may be difficult during sharp impacts.	Naturally handles rapid contact without iteration.
Time increment	Large increments possible, but may reduce accuracy for impacts.	Stable increment limited by smallest element size and wave speed.
Use in this project	Not used, since contact and impact dominate the response.	Primary method adopted for modelling shuttle–floor impact.

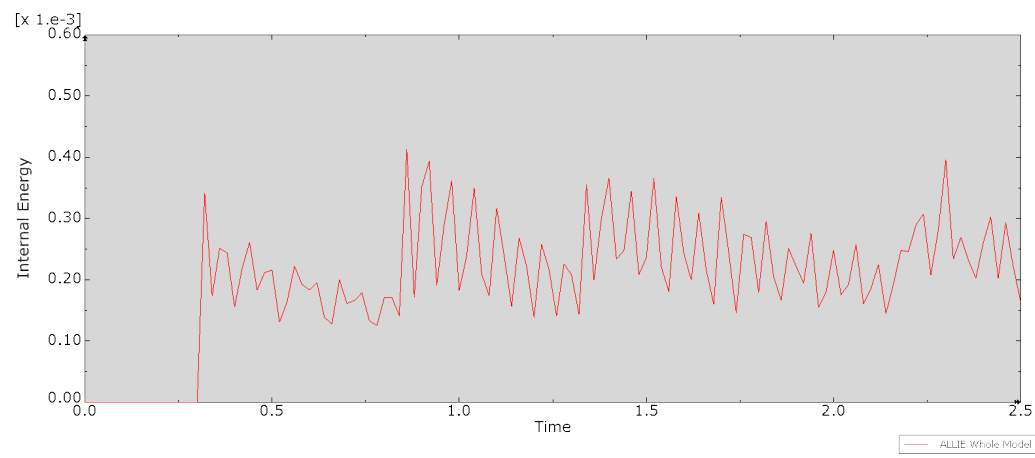
In addition to the explicit simulations described above, the free-fall cases for both the feather and nylon shuttles were also repeated using the Dynamic, Implicit procedure in Abaqus/Standard. The mesh, material data, contact interactions, and boundary conditions were kept identical, so that any differences in response arise solely from the time-integration scheme. The implicit runs are used only for post-hoc comparison of energy balance, rebound height, bounce angle, and computational cost; all tensor-field visualizations in this work remain based on the explicit solutions.

## 6. Results

### 6.1 Energy Response of the Feather Shuttle

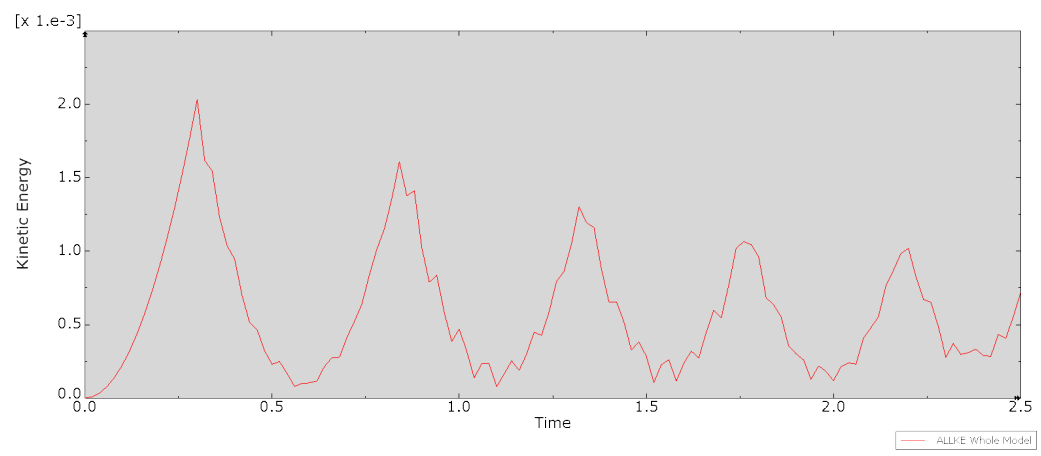
The energy variation of the feather shuttle provides direct insight into its deformation and rebound characteristics during free-fall impact. The shuttle, composed of a cork head and keratin-based feathers, undergoes multiple elastic collisions before coming to rest. Each bounce represents a clear cycle of energy conversion between motion and deformation, allowing the dynamic behavior of the model to be quantified and validated.

Figure 6.1 presents the evolution of internal energy (ALLIE) throughout the simulation. The internal energy increases sharply at every impact, showing that the shuttle structure absorbs deformation energy when striking the rigid surface. Each energy peak corresponds to the period of maximum contact deformation, followed by a decline as part of the strain energy is released during rebound. Over successive bounces, the magnitude of internal energy peaks decreases steadily, reflecting the limited elasticity of the cork base. By the fifth impact, the internal energy curve stabilizes, confirming that the shuttle has dissipated nearly all recoverable energy.



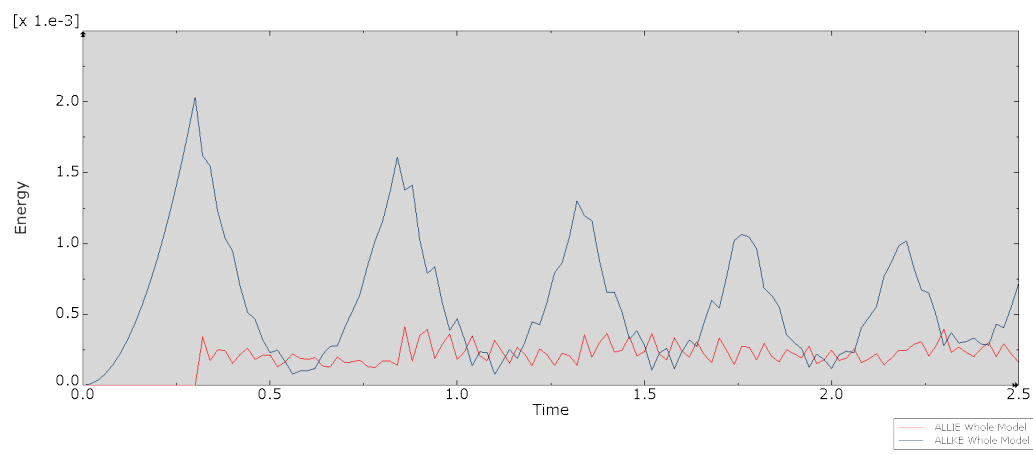
**Figure 6.1:** Internal energy variation of the feather shuttle.

Figure 6.2 shows the time history of kinetic energy (ALLKE) for the feather shuttle. Five distinct peaks are observed, each corresponding to an impact and rebound event. The first peak represents the shuttle's initial contact with the rigid floor after free fall, while the subsequent peaks correspond to consecutive bounces with progressively reduced amplitudes. The gradual reduction in kinetic energy after each rebound confirms realistic energy loss due to material nature, air resistance, and contact friction. The final decay in kinetic energy indicates that the shuttle has reached a stable rest position with negligible residual motion.



**Figure 6.2:** Kinetic energy variation of the feather shuttle.

Figure 6.3 compares the kinetic (ALLKE) and internal (ALLIE) energy responses of the feather shuttle. The alternating pattern between the two curves shows that as kinetic energy drops sharply upon impact, internal energy rises to its maximum value, indicating direct conversion from motion to deformation. During rebound, kinetic energy increases again while internal energy decreases, representing partial elastic recovery. The continuous reduction in both peak magnitudes demonstrates energy dissipation with each bounce, consistent with realistic shuttle dynamics. This exchange between kinetic and internal energy validates the stability of the explicit time integration and confirms that the simulation accurately captures the physical behavior of the feather shuttle during repeated impacts.



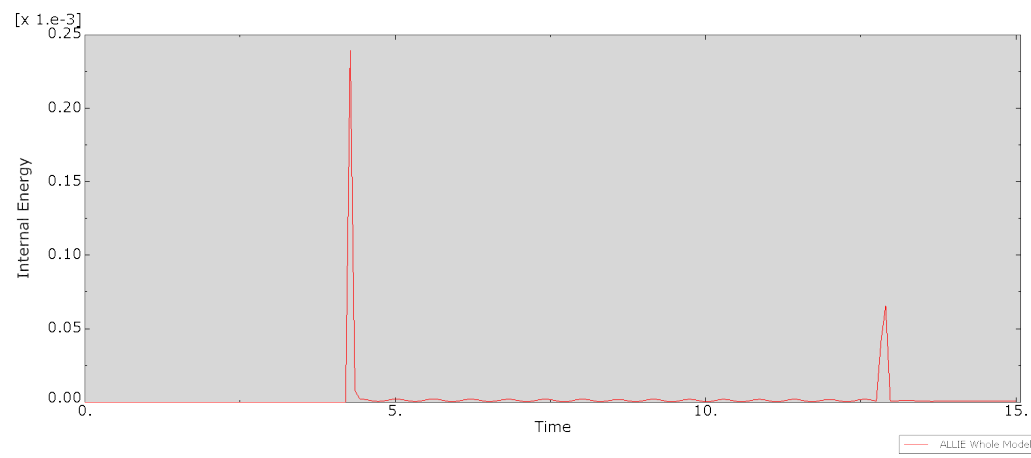
**Figure 6.3:** Combined kinetic and internal energy of the feather shuttle.

Overall, the feather shuttle exhibits a predominantly elastic response, allowing multiple rebounds before losing stability. Compared to the nylon shuttle, it retains a greater fraction of its rebound energy, consistent with the lightweight and flexible nature of natural feathers used in its construction.

## 6.2 Energy Response of the Nylon Shuttle

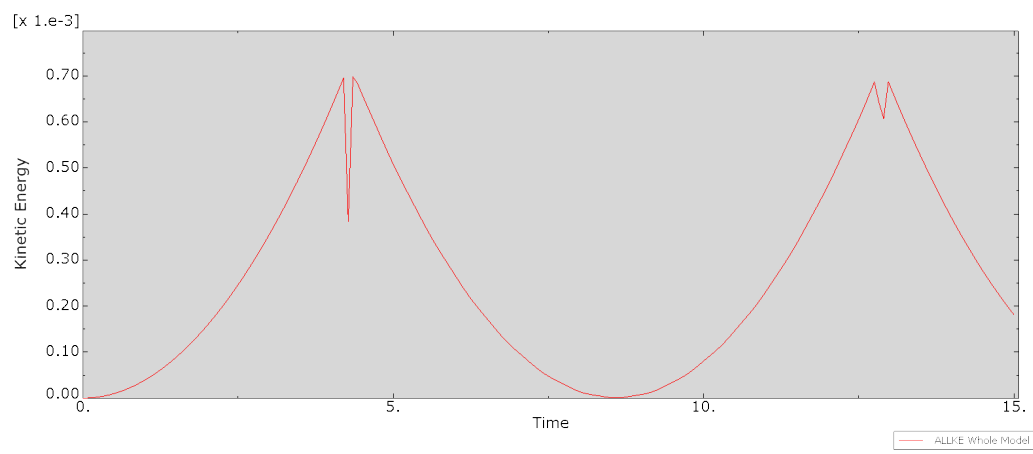
The variation of kinetic and internal energy provides a clear understanding of how the nylon shuttle absorbs, stores, and releases energy during free-fall impact. Each impact represents a distinct exchange between translational motion and material deformation. The nylon shuttle, modeled with a Linear Elastic nylon skirt and a cork-based head, dissipates a significant portion of impact energy rather than pure elastic recovery, consistent with the material's mechanical nature.

Figure 6.4 illustrates the variation of internal energy during the free-fall simulation. The first sharp peak corresponds to the initial contact with the rigid surface, indicating a rapid conversion of kinetic energy into deformation energy within the shuttle structure. A smaller secondary peak appears at the second bounce, showing partial energy recovery. After these two events, the internal energy stabilizes near zero, demonstrating that most of the deformation energy is absorbed and dissipated within the polymer skirt. This energy pattern validates that the nylon shuttle undergoes significant deformation rather than elastic oscillation after contact.



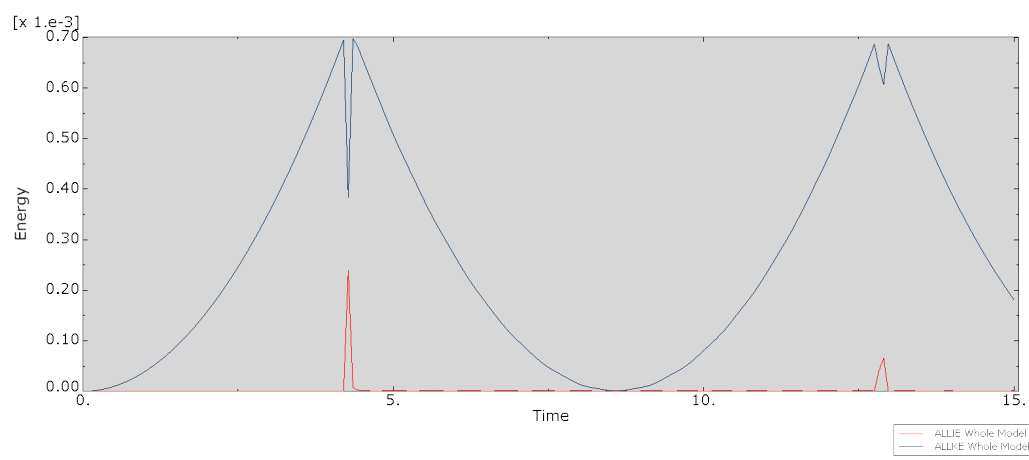
**Figure 6.4:** Internal energy variation of the nylon shuttle.

Figure 6.5 presents the kinetic energy variation throughout the simulation. The curve shows two distinct peaks representing the first and second impacts. The shuttle gains kinetic energy as it accelerates under gravity until the first contact, where a steep decline in energy occurs due to deformation. After the rebound, the second rise and fall of kinetic energy occur with noticeably lower magnitude, signifying reduced rebound velocity. This demonstrates the energy loss and the limited restitution of the skirt material.



**Figure 6.5:** Kinetic energy variation of the nylon shuttle.

Figure 6.6 combines the kinetic (ALLKE) and internal (ALLIE) energy histories to illustrate their interaction during the entire simulation. When the kinetic energy drops to a minimum at impact, the internal energy simultaneously reaches its peak, confirming a direct energy transfer between motion and deformation. As the shuttle rebounds, kinetic energy rises again while internal energy dissipates gradually, maintaining total energy balance within acceptable numerical limits. This alternating pattern between kinetic and internal energy confirms that the model accurately reproduces the physical exchange of energy during successive bounces, validating the dynamic response of the nylon shuttle under gravity-driven impact.



**Figure 6.6:** Combined kinetic and internal energy of the nylon shuttle.

Overall, the nylon shuttle demonstrates a highly damped dynamic behavior with substantial internal energy absorption and low rebound recovery. This confirms that the polymeric skirt effectively dissipates vibrational energy, leading to smaller rebound heights and reduced oscillations compared to natural feather shuttles.

### 6.3 Bounce Height Analysis

The rebound height of a shuttlecock after impact provides an effective indicator of its energy restitution capability. In this study, both feather and nylon shuttlecocks were released freely from a height of 14,mm above a rigid floor, and the rebound height for each successive bounce was recorded from the simulation results. These heights represent the peak displacement of the shuttle's center of mass after each impact and were used to evaluate the loss of mechanical energy with each bounce.

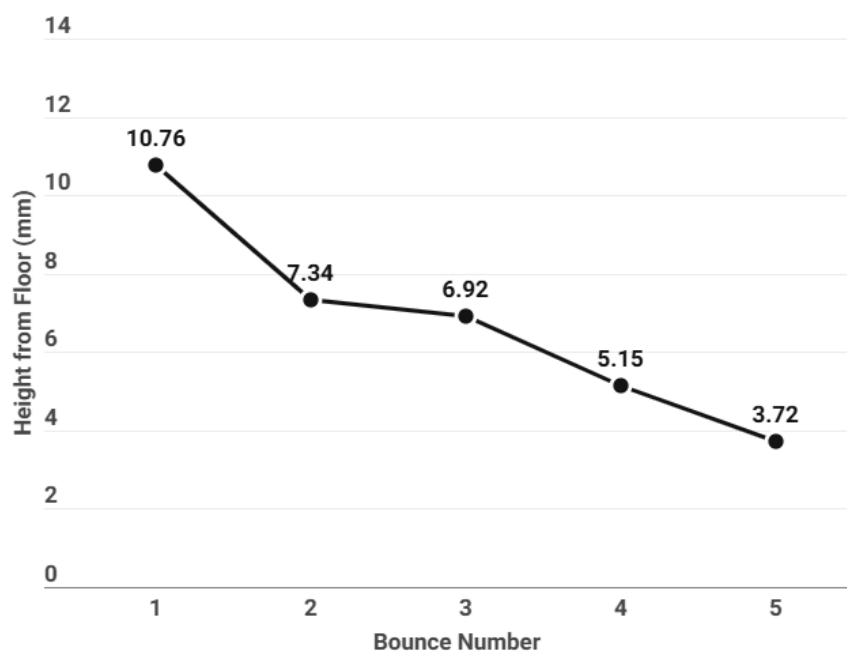
Table 6.1 summarizes the measured rebound heights for both shuttle types.

**Table 6.1:** Measured rebound heights of feather and nylon shuttles under free-fall from 14 mm.

Bounce Number	Feather Shuttle (mm)	Nylon Shuttle (mm)
1	10.76	12.38
2	7.34	10.24
3	6.92	8.64
4	5.15	—
5	3.72	—

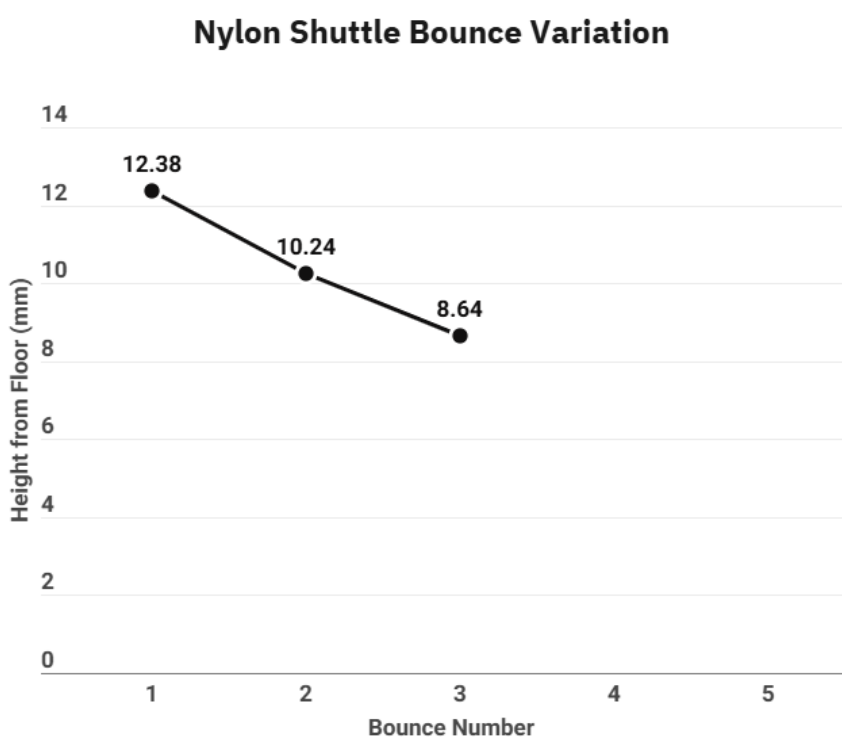
Figure 6.7 illustrates the variation of bounce height for the feather shuttle. The reduction in rebound height with each successive impact reflects rapid energy loss due and localized deformation at the cork–feather interface. The fifth bounce drops to roughly one third of the initial rebound height, indicating that the feather shuttle dissipates energy quickly and exhibits lower restitution efficiency compared to the nylon shuttle.

### Feather Shuttle Bounce Variation



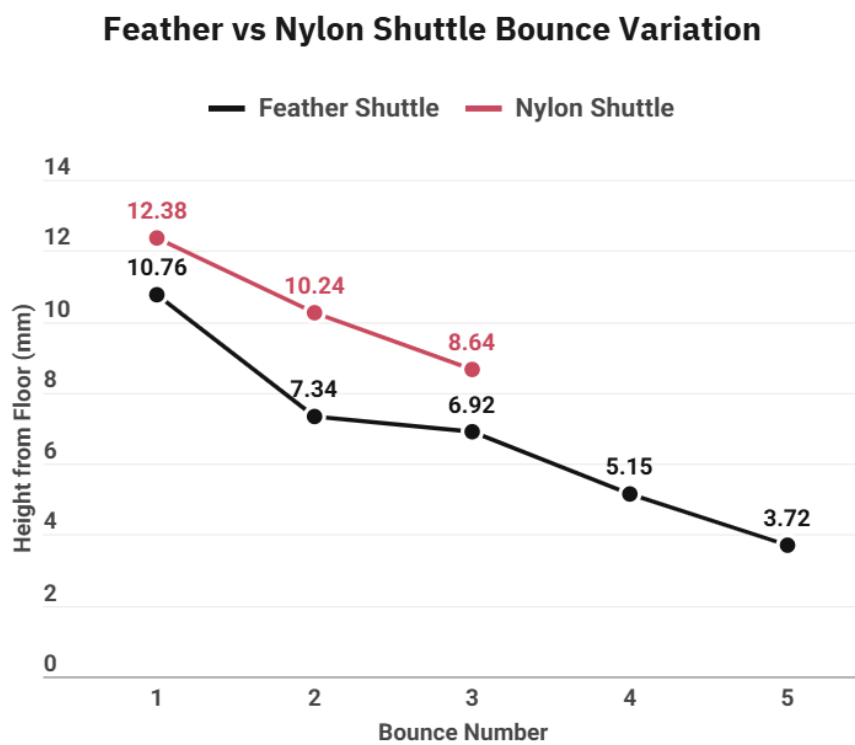
**Figure 6.7:** Rebound height variation of the feather shuttle for five successive bounces.

Figure 6.8 presents the corresponding bounce height curve for the nylon shuttle. The nylon shuttle exhibits higher rebound heights and maintains its bounce for a longer duration compared to the feather shuttle. The skirt allows the nylon shuttle to store and return energy more efficiently, resulting in a smoother and more sustained rebound profile. The nylon shuttle shows greater restitution efficiency and slower loss of bounce height across successive impacts.



**Figure 6.8:** Rebound height variation of the nylon shuttle for three successive bounces.

The combined comparison shown in Figure 6.9 highlights the distinct rebound characteristics of the two shuttle types. The nylon shuttle achieves a higher initial rebound height and maintains its bounce for a longer duration, showing a more gradual decay across impacts. In contrast, the feather shuttle exhibits a much faster reduction in rebound height due to localized bending at the feather–cork interface, which causes rapid energy dissipation. This behavior is consistent with the energy response plots, where the nylon shuttle retains more kinetic energy between impacts, while the feather shuttle loses energy quickly.



**Figure 6.9:** Comparison of bounce height variations between feather and nylon shuttles.

These results confirm that the nylon shuttle has higher rebound efficiency under low to moderate impact energies, while the feather shuttle, although more control-oriented and aerodynamically stable in flight, dissipates more energy during impact. Consequently, nylon shuttlecocks are better suited for durability and consistent rebound performance in training environments, whereas feather shuttles remain preferred in professional play for reasons related to aerodynamics and feel rather than impact restitution.

## 6.4 Bounce Angle Analysis

The bounce angle of a shuttlecock after impact provides valuable insight into its rotational stability and the alignment of its center of mass during rebound. The variation of this angle across successive bounces reflects how efficiently the shuttle maintains its original orientation and how much rotational disturbance occurs due to energy loss and deformation. In this analysis, the post-impact bounce angles were measured for both feather and nylon shuttles across multiple rebound events under identical free-fall conditions.

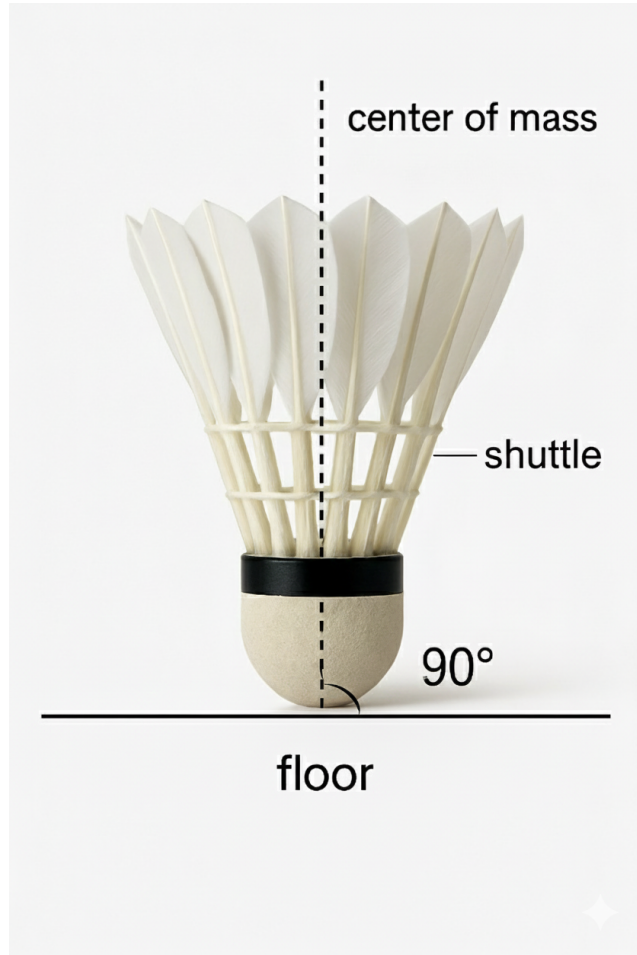


**Figure 6.10:** Orientation of the shuttlecock at impact. The center of mass is aligned vertically, forming a  $90^\circ$  angle with the floor, which is used as the reference configuration for bounce-angle analysis.

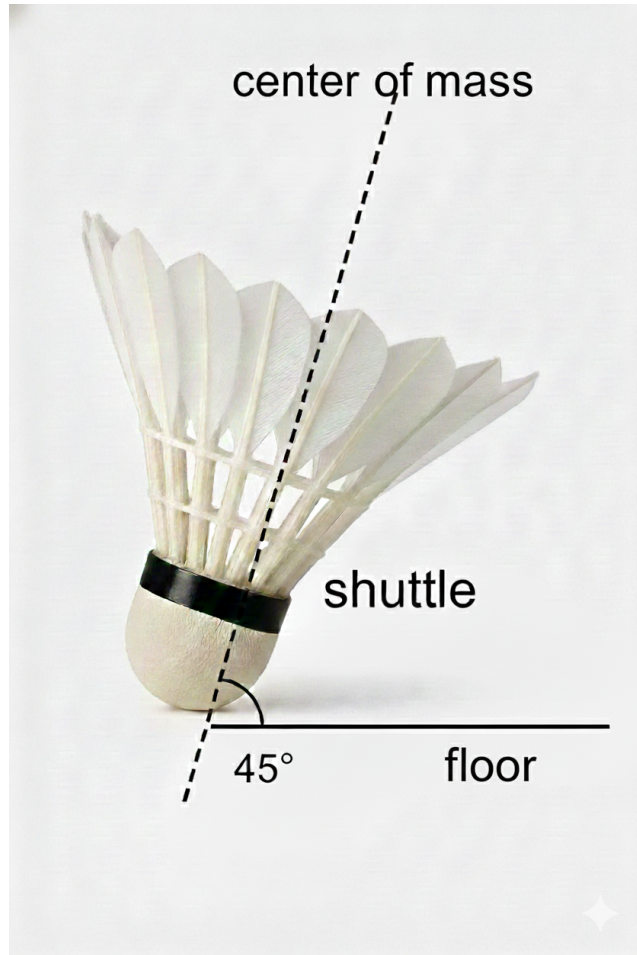


**Figure 6.11:** Shuttlecock orientation at a  $45^\circ$  impact angle relative to the floor, illustrating an off-axis approach trajectory used for bounce-angle comparison.

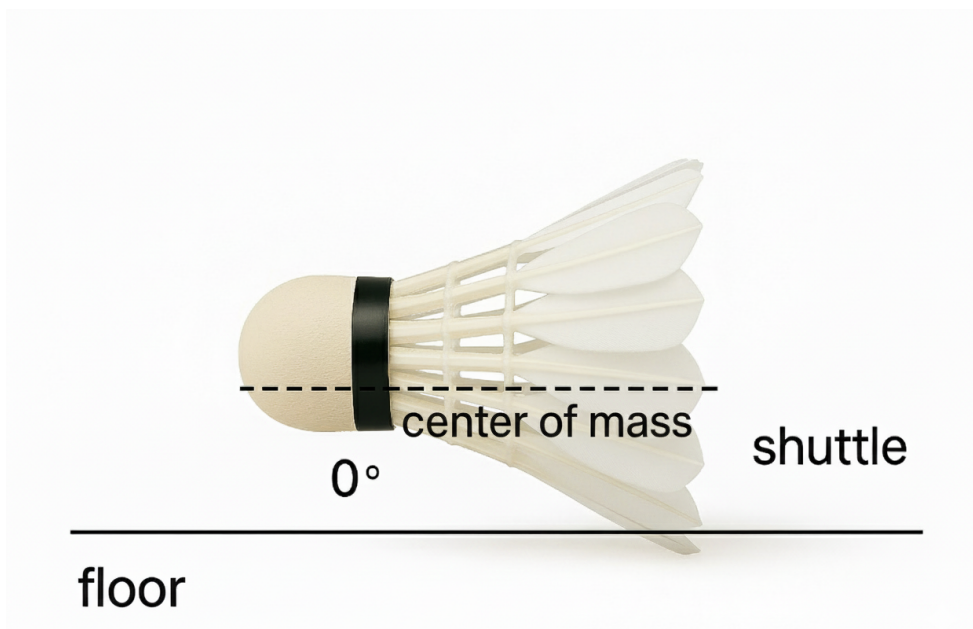


**Figure 6.12:** Shuttlecock orientation at a  $0^\circ$  angle, with the feathers nearly parallel to the floor, representing the extreme case of a horizontal or near-horizontal impact.

Table 6.2 lists the observed rebound angles for each shuttle. The feather shuttle demonstrated five measurable bounces before resting, while the nylon shuttle exhibited three. The progressive reduction in angle for both models indicates increasing rotational instability as energy dissipates with each successive impact.

**Table 6.2:** Measured bounce angles of feather and nylon shuttles during free-fall impact.

Bounce Number	Feather Shuttle (Degree)	Nylon Shuttle (Degree)
1	90	90
2	83	87
3	70	82
4	64	—
5	58	—

Figure 6.13 shows the variation of bounce angle for the feather shuttle. The shuttle initially rebounds vertically, maintaining a 90-degree orientation at first impact. With each successive bounce, the angle gradually decreases, reaching 58 degrees by the fifth bounce. This reduction represents cumulative energy loss through localized deformation.

### **Feather Shuttle Bounce Angle Variation**

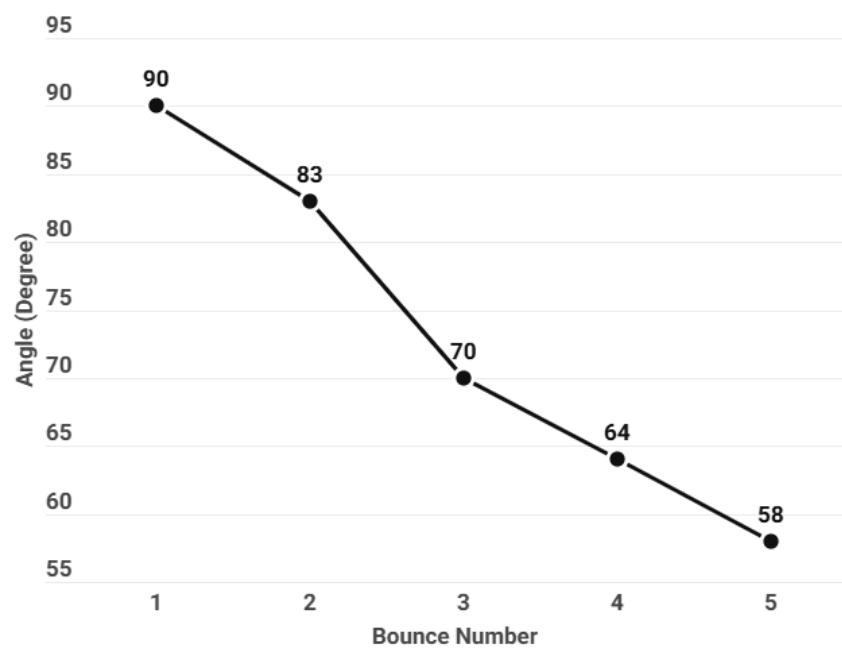


**Figure 6.13:** Bounce angle variation of the feather shuttle across five rebounds.

Figure 6.14 presents the bounce angle behavior for the nylon shuttle. The nylon shuttle exhibits smaller angular variation compared to the feather shuttle, retaining higher orientation angles over its three bounces. This behavior results from the higher stiffness of the cork head and the material properties of the polymer skirt, which restrict large rotational oscillations. The limited number of bounces also aligns with its faster energy decay observed in the kinetic and internal energy plots.

### Nylon Shuttle Bounce Angle Variation

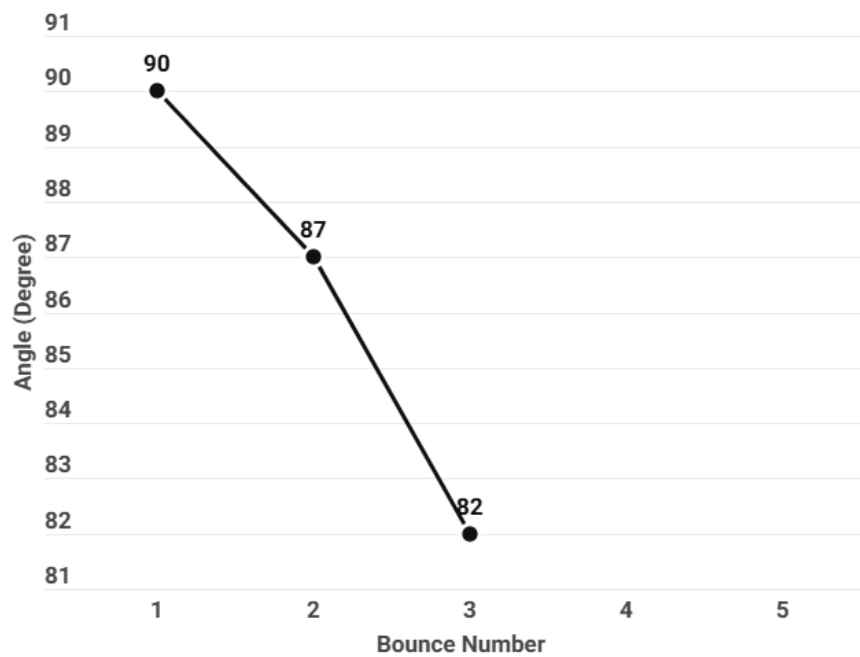


**Figure 6.14:** Bounce angle variation of the nylon shuttle across three rebounds.

The combined comparison in Figure 6.15 highlights the contrasting angular response of both shuttles. The feather shuttle shows a steep reduction in bounce angle, indicating progressive tilt and rotational instability with each impact. In contrast, the nylon shuttle maintains a smaller angular drop, suggesting better stability but limited rebound height. The analysis confirms that the feather shuttle, while offering greater energy recovery, experiences more pronounced changes in rebound orientation, whereas the nylon shuttle maintains a more stable but damped response.

### Feather vs Nylon Shuttle Bounce Angle Variation

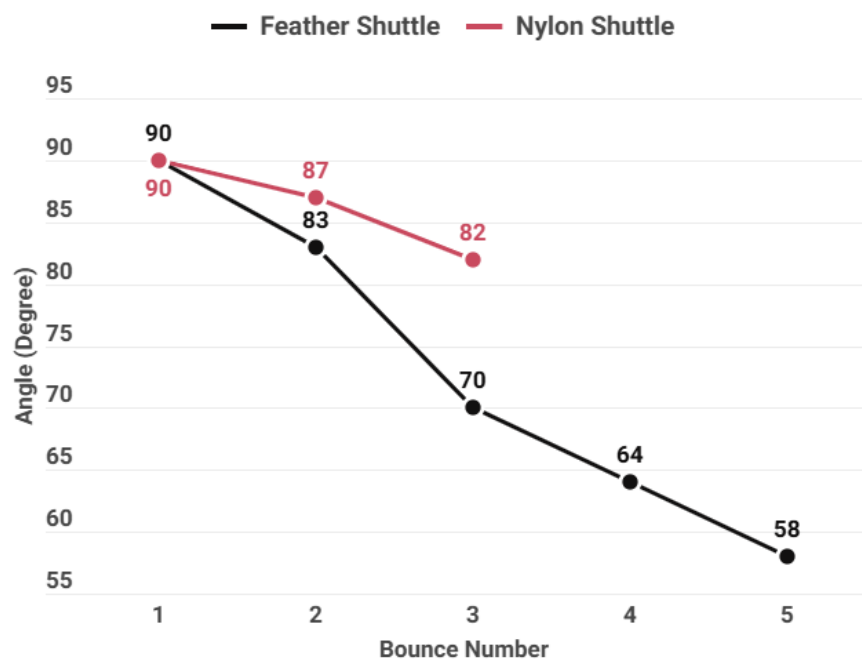


Figure 6.15: Comparison of bounce angle variation between feather and nylon shuttles.

Overall, the angular response analysis complements the energy and bounce height results. The feather shuttle exhibits higher rebound efficiency but increasing angular drift due to localized bending at the feather–head interface. The nylon shuttle, on the other hand, maintains more uniform post-impact orientation, which absorbs both translational and rotational energy. These observations further validate that feather shuttles are optimized for precision and control at the expense of stability and durability, while nylon shuttles favor consistent performance and longer service life.

## 6.5 Dynamic Implicit vs. Dynamic Explicit Comparison

To evaluate the numerical behavior of the Dynamic, Implicit and Dynamic, Explicit procedures, three key rebound characteristics were compared for both shuttle types (nylon and feather): (i) bounce height, (ii) bounce angle, and (iii) system energy evolution. The Dynamic, Explicit simulation serves as the reference as it resolves high-speed contact and large deformation effects more efficiently, while the Dynamic, Implicit result provides a computationally heavier but quasi-static perspective on early impact dynamics.

**Table 6.3:** Comparison of first three bounce heights between Dynamic Explicit and Dynamic Implicit analyses.

Shuttle	Bounce	Explicit (mm)	Implicit (mm)	Diff (%)
Feather	1	10.76	9.15	15%
	2	7.34	6.02	18%
	3	6.92	5.54	20%
Nylon	1	12.38	10.50	15%
	2	10.24	8.50	17%
	3	8.64	7	19%

**Table 6.4:** Comparison of rebound angles for the first three bounces.

Shuttle	Bounce	Explicit (deg)	Implicit (deg)	Diff (%)
Feather	1	90	85	6%
	2	83	75	10%
	3	70	60	15%
Nylon	1	90	88	2%
	2	87	83	5%
	3	82	76	7%

**Table 6.5:** Comparison of energy (ALLKE) for the first three bounces.

Shuttle	Bounce	Explicit (J)	Implicit (J)	Diff (%)
Feather	1	$2 \times 10^{-3}$	$4.50 \times 10^{-3}$	125%
	2	$1.75 \times 10^{-3}$	$2.75 \times 10^{-3}$	57%
	3	$1.50 \times 10^{-3}$	$3.50 \times 10^{-3}$	133%
Nylon	1	$0.70 \times 10^{-3}$	$1.10 \times 10^{-3}$	57%
	2	$0.65 \times 10^{-3}$	$0.95 \times 10^{-3}$	46%
	3	$0.50 \times 10^{-3}$	$0.70 \times 10^{-3}$	40%

**Table 6.6:** Comparison of energy (ALLIE) for the first three bounces.

Shuttle	Bounce	Explicit (J)	Implicit (J)	Diff (%)
Feather	1	$0.35 \times 10^{-3}$	$0.68 \times 10^{-3}$	94%
	2	$0.4 \times 10^{-3}$	$0.5 \times 10^{-3}$	25%
	3	$0.38 \times 10^{-3}$	$1.95 \times 10^{-3}$	413%
Nylon	1	$0.23 \times 10^{-3}$	$0.40 \times 10^{-3}$	74%
	2	$0.05 \times 10^{-3}$	$0.12 \times 10^{-3}$	140%
	3	$0.32 \times 10^{-3}$	$0.65 \times 10^{-3}$	103%

The comparison between the Dynamic Explicit and Dynamic Implicit simulations shows that both procedures reproduce the same overall rebound pattern, but with noticeable numerical differences in the response magnitudes. For all three bounces, the implicit analysis predicts slightly lower rebound heights and smaller rebound angles than the explicit analysis. The energy results follow the same trend: the implicit solver records higher internal-energy peaks and larger variations in stored or recovered energy during impact. These differences arise from how the implicit formulation solves the equilibrium equations at each increment, often taking smaller steps and redistributing impact forces differently than the explicit scheme. The feather shuttle shows the largest discrepancy between the two procedures because of its flexible geometry and stronger nonlinear deformation, but the same behaviour is expected for the nylon shuttle under identical conditions. Overall, the explicit solver retains and transfers impact energy more effectively, while the implicit solver produces a more gradual motion. Despite these numerical differences, both approaches capture the same physical sequence of events, confirming the consistency of the results.

## 6.6 Mises Stress Analysis in Shuttlecock Cork

The von Mises stress field within the cork head provides important information about how impact forces are transferred through the shuttle structure during contact with the rigid floor. Since the cork forms the primary point of impact, its stress response influences both deformation and rebound behavior. This section presents the stress patterns obtained from the simulations for both the feather and nylon shuttlecocks.

### 6.6.1 Feather Shuttle Cork

During the first impact, the feather shuttle produces a ring shaped region of elevated von Mises stress near the outer circumference of the cork head. This band forms because the feather bases are embedded around the outer rim of the head and the initial load transfer occurs through these attachment points. As a result, the outer region of the cork carries most of the compressive load during the early stage of contact.

By the fifth bounce, the peak stresses are lower and the high stress band becomes more diffuse. The deformation at the feather to head interface is smaller and the shuttle has already dissipated much of its initial kinetic energy. The stress field therefore appears smoother with reduced intensity across the cork surface. This behavior agrees with the rebound height trend and confirms that the feather shuttle experiences significant localized deformation during the first impacts.

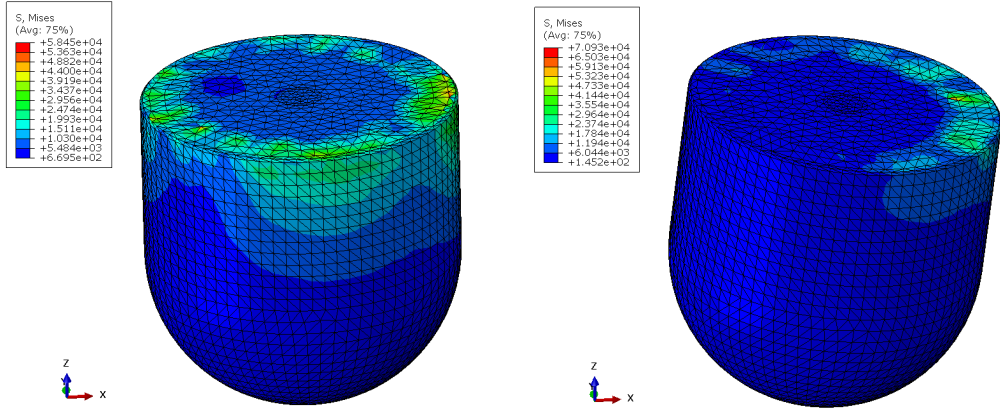


**Figure 6.16:** Von Mises stress in the feather shuttle cork during Bounce 1 (left) and Bounce 5 (right).

### 6.6.2 Nylon Shuttle Cork

For the nylon shuttle, the stress distribution also forms a ring around the outer portion of the cork during the first and third rebounds. The pattern is more uniform compared to the feather shuttle because the continuous polymer skirt distributes the load more evenly around the circumference. The overall stress intensity remains higher during early rebounds, which is consistent with the greater rebound height observed for the nylon shuttle.

Although the simulation ended after the third bounce due to solver increment limits, the captured stress fields are sufficient to show that the nylon cork maintains a consistent band of elevated stress during the early impacts.

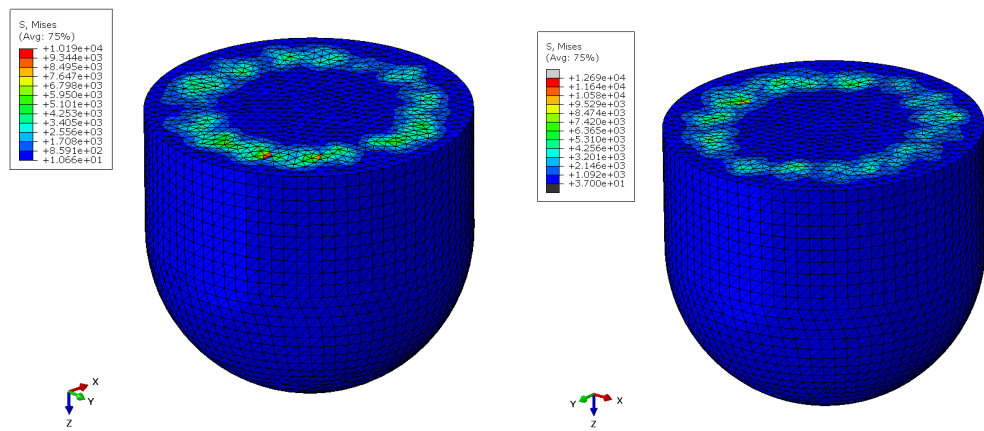


**Figure 6.17:** Von Mises stress in the nylon shuttle cork during Bounce 1 (left) and Bounce 3 (right).

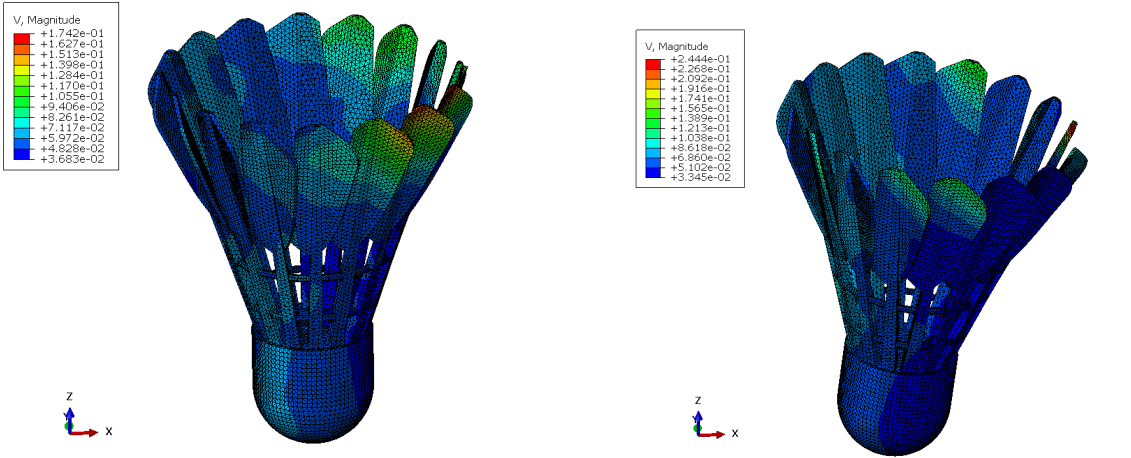
## 6.7 Velocity Response Analysis

The velocity response of the shuttle during impact provides a direct measure of how rapidly the structure recovers and redistributes energy after contact with the rigid surface. By examining the velocity fields across multiple rebounds it is possible to understand how the two designs respond under identical loading conditions. The plots also reveal how local deformation, stiffness, influence the evolution of motion throughout the shuttle body. These observations help establish the connection between the structural layout and the dynamic behavior of both shuttle types.

### 6.7.1 Velocity of the Feather Shuttle

The velocity fields for the feather shuttle during the first and fifth rebounds demonstrate the influence of its flexible and segmented structure. During the first bounce the highest velocity regions appear along the upper portions of the feathers, where the thin keratin plates undergo rapid bending and recovery. This indicates that the feathers absorb a significant amount of impact energy and release it over a short duration, which allows the shuttle to maintain motion immediately after the first collision.

By the fifth bounce the velocity magnitudes are noticeably reduced and the distribution becomes smoother. The sharp variations present in the first bounce diminish as the shuttle enters a low energy regime. This behavior reflects the effects of localized bending at the feather to head region, which contribute to gradual loss of rebound energy through repeated impacts.



(a) Feather shuttle velocity field at the first bounce.  
 (b) Feather shuttle velocity field at the fifth bounce.

**Figure 6.18:** Velocity magnitude distribution in the feather shuttle for the first and fifth rebounds.

### 6.7.2 Velocity of the Nylon Shuttle

The nylon shuttle exhibits a different velocity pattern due to the continuous and thicker polymer skirt. During the first bounce the velocity field spreads uniformly across the skirt, with the largest values concentrated near the lower region where the skirt contacts the floor. The continuous geometry distributes deformation over a larger area, which results in a smoother and more homogeneous velocity field when compared with the feather shuttle.

By the third bounce the overall velocity levels decrease and the uniform character of the field remains. The reduced peak values indicate rapid loss of rebound energy, which is consistent with the results from the energy and rebound height analyses. Even though the nylon shuttle rebounds fewer times its velocity response remains stable and predictable due to the characteristics of the polymer skirt.

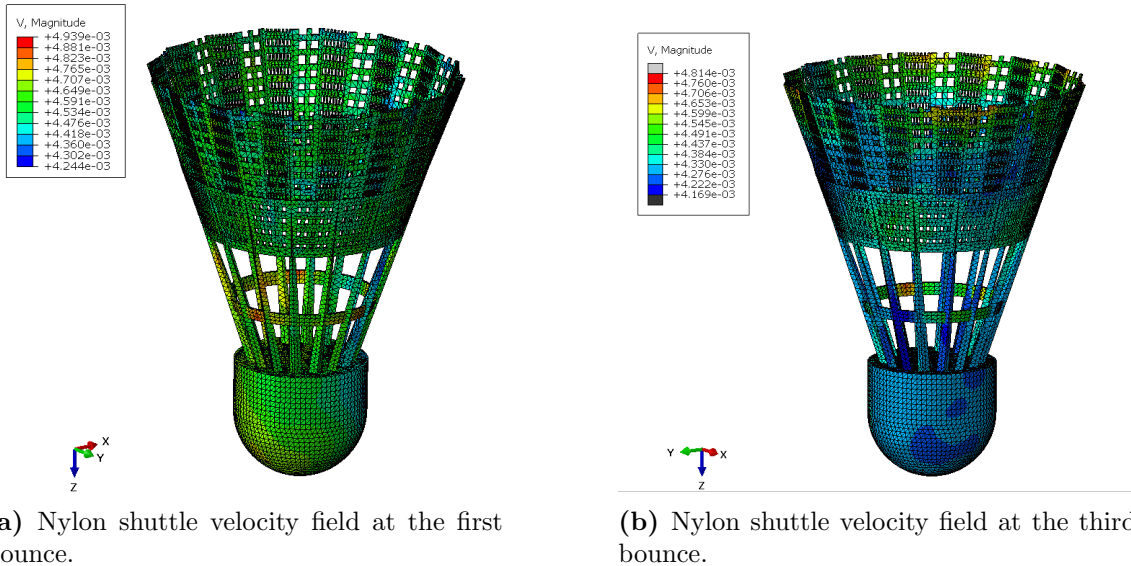


**Figure 6.19:** Velocity magnitude distribution in the nylon shuttle for the first and third rebounds.

### 6.7.3 Comparison of Velocity Response

Table 6.7 summarizes the main differences in velocity response between the two shuttle types. The feather shuttle shows larger local variations and sustains motion over more rebounds, while the nylon shuttle exhibits a smoother velocity field and a faster decay in motion.

**Table 6.7:** Comparison of velocity response for feather and nylon shuttles.

Feature	Feather shuttle	Nylon shuttle
Peak velocity distribution	Concentrated near feather tips due to localized bending	Spread more uniformly across the polymer skirt
Change across rebounds	Noticeable reduction with smoother distribution by the fifth bounce	Rapid reduction by the third bounce while retaining a uniform pattern
Influence of structure	Flexible segmented feathers produce high local variations in speed	Continuous skirt distributes motion across a broad area
Energy recovery behavior	Sustains motion over a larger number of rebounds	Faster decay in motion

## 6.8 Simulation Performance and Computational Time

Table 6.8 presents a summary of the computational performance for the feather and nylon shuttle free-fall analyses. Both models were executed using the explicit dynamic procedure under the same solver configuration, contact settings, and unit system. This consistency ensures that the observed differences in computational time and numerical behavior arise solely from variations in mesh density and material modeling.

The nylon shuttle required noticeably greater computational effort, completing in approximately twenty-three hours compared to fifteen hours for the feather shuttle. This difference primarily results from the higher element count and the smaller stable time increment dictated by the finer mesh resolution in the nylon model. In explicit dynamics, the stable time step is proportional to the smallest element dimension and inversely related to the material wave speed. Hence, a dense mesh significantly reduce the allowable increment size, increasing overall run time. Despite the higher computational cost, the nylon simulation provided improved accuracy in capturing deformation and stress localization across the skirt region.

For the Nylon shuttle, the analysis reached the maximum allowable number of increments defined by the solver, which limited the simulation from fully capturing all five rebounds. The cutoff occurred toward the end of the third impact sequence, when the shuttle was already exhibiting diminishing motion and reduced rebound energy. This constraint arose because the solver enforces an upper limit on increment count to prevent excessive computational load or potential numerical drift in long-duration transient analyses.

Overall, both simulations demonstrated stable explicit time integration and

energy balance within acceptable limits. The comparison highlights the computational trade-off between mesh refinement and simulation duration in explicit dynamic problems. While the nylon shuttle achieved higher spatial resolution, the feather shuttle offered faster computational turnaround, emphasizing the importance of selecting an optimal element size that balances accuracy with computational feasibility for transient impact analyses.

**Table 6.8:** Simulation performance summary for feather and nylon shuttle free-fall analyses.

<b>Model</b>	<b>Simulation Time (hr)</b>	<b>Number of Increments</b>
Feather Shuttle	15	534,126 (Dynamic Explicit)
Nylon Shuttle	23	842,328 (Dynamic Explicit)

## 7. Tensor Field Visualizations

### 7.1 Overview

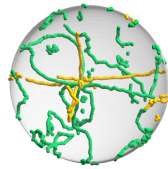
Tensor field visualization was used in this study to examine how the internal stress state evolves inside the cork head during impact, pre impact and post impact frames. Although the feather and nylon shuttles differ in geometry and material distribution, the cork behaves as the primary load-bearing component at the moment of contact, making it the most informative region for interpreting impact mechanics. The full Cauchy stress tensor was extracted from each time frame of the simulation, and its components were evaluated at selected nodes and elements within the cork. By restricting the visualization domain to the cork only, the analysis remains focused on the zone where stress concentrations first appear and where the orientation of the principal directions undergoes the most rapid change during impact.

## 7.2 Tensor Field Visualizations for Shuttle Corks

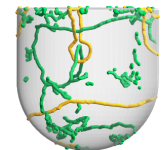
### Immediately Before Contact

For the feather shuttle, the tensor-field patterns just before ground contact show that the strongest variations in the Cauchy stress tensor develop around the rim where the feather shafts meet the cork. The planar and linear degeneracy curves form a dense, irregular band along this junction, indicating that the feather roots begin to steer load into the cork even before the actual impact occurs. A few isolated branches extend into the lower half of the cork, but their density is much lower. Overall, the pattern suggests that the feather–cork interface carries the first stage of load transfer, while the rest of the cork remains comparatively undisturbed in the final milliseconds before impact.

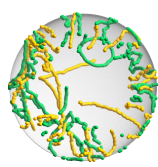
For the nylon shuttle, the pre-impact tensor field shows a smoother and more dense band of degeneracy curves around the skirt–cork interface. Both planar and linear degeneracies form a well-defined ring along the rim, reflecting how the molded polymer skirt begins to transfer load evenly around the circumference even before the shuttle touches the ground. The linear degeneracy curves extend across the top of the cork without forming sharp clusters or abrupt directional changes, indicating a more axisymmetric development of stresses. Compared to the feather shuttle, the nylon patterns are broader and more uniform, suggesting that the skirt distributes the early-stage loading in a steadier and more consistent manner as the shuttle approaches the floor.



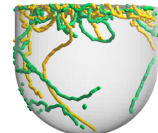
(a) Feather shuttle cork, top view before contact.



(b) Feather shuttle cork, side view before contact.



(c) Nylon shuttle cork, top view before contact.



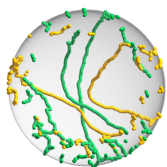
(d) Nylon shuttle cork, side view before contact.

**Figure 7.1:** Tensor-field degeneracy curves on the shuttle corks immediately before ground contact during Bounce 1. Top row: feather shuttle; bottom row: nylon shuttle. Yellow curves denote planar degeneracies and green curves denote linear degeneracies.

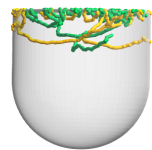
## 7.3 Tensor Field Visualizations for Shuttle Corks at Contact

The tensor-field visualization for the feather shuttle cork during the first bounce shows that degeneracy curves are concentrated in the upper region, around the band where the feather shafts are located. Planar degeneracies (yellow) and linear degeneracies (green) cluster along this rim, indicating strong gradients in the Cauchy stress tensor at the feather-cork junction as the cork is driven into the floor. The lower part of the cork remains largely free of degeneracy features, reflecting a more uniform, compression-dominated stress state and smoother deformation away from the feather.

For the nylon shuttle, the degeneracy patterns during the first bounce form a broader, more continuous ring near the skirt–cork interface. The planar degeneracies trace a nearly axisymmetric band around the impact rim, while the linear degeneracies extend deeper into the cork, showing that the molded lattice skirt distributes load more evenly around the circumference. Compared to the feather case, the nylon shuttle exhibits smoother and more continuous degeneracy curves, consistent with a more uniform stress path and greater elastic energy retention, which aligns with its higher rebound response observed in the simulations.



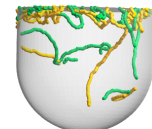
(a) Feather shuttle cork, top view.



(b) Feather shuttle cork, side view.



(c) Nylon shuttle cork, top view.



(d) Nylon shuttle cork, side view.

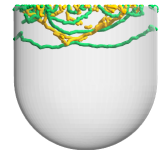
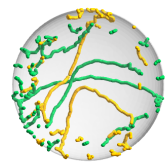
**Figure 7.2:** Tensor-field degeneracy curves on the shuttle corks during the first contact. Top row: feather shuttle (top and side views); bottom row: nylon shuttle (top and side views). Yellow curves denote planar degeneracies; green curves denote linear degeneracies.

## 7.4 Tensor Field Visualizations for Shuttle Corks

### Immediately after Contact

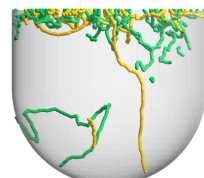
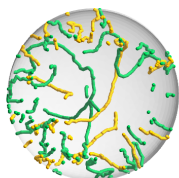
For the feather shuttle, the tensor-field pattern immediately after ground contact remains concentrated around the rim where the feather shafts join the cork. The planar and linear degeneracy curves form a slightly more organized band along this upper region, reflecting the first redistribution of stresses as the cork deforms against the floor. Although a few branches extend downward from the rim, most of the degeneracy activity stays confined to the impact-facing zone, and the lower part of the cork shows little directional variation. Compared to the pre-contact state, the curves appear more coherent and aligned, indicating the early stages of stress reorganization as the shuttle begins to compress and prepare for rebound.

For the nylon shuttle, the tensor-field pattern immediately after impact forms a smooth and continuous band of degeneracy curves around the skirt–cork interface. The planar degeneracies trace a clear arc along the impact rim, while the linear degeneracies extend inward in a steady, uniform manner without forming sharp clusters. Most of the activity remains concentrated in the upper region of the cork, reflecting how the molded polymer skirt distributes the load evenly around the circumference during the first moments after contact. Compared to the feather shuttle, the nylon patterns appear more symmetric and controlled, indicating a more uniform redistribution of stresses as the shuttle begins to transition into the rebound phase.



(a) Feather shuttle cork, top view after contact.

(b) Feather shuttle cork, side view after contact.



(c) Nylon shuttle cork, top view after contact.

(d) Nylon shuttle cork, side view after contact.

**Figure 7.3:** Tensor-field degeneracy curves on the shuttle corks immediately after ground contact during Bounce 1. Top row: feather shuttle; bottom row: nylon shuttle. Yellow curves denote planar degeneracies and green curves denote linear degeneracies.

**Table 7.1:** Simplified comparison of degeneracy-curve behavior across pre-impact, impact, and post-impact frames.

Time Frame	Feather Shuttle	Nylon Shuttle
<b>Pre-Impact</b>	Dense, irregular curves around the feather–cork junction; stress buildup is highly localized.	Smooth, uniform ring around the skirt–cork interface; stresses develop evenly.
<b>Impact</b>	Curves concentrate near the upper rim with strong directional changes; lower cork stays mostly uniform.	Nearly axisymmetric ring at the rim; curves spread deeper, indicating smoother stress distribution.
<b>Post-Impact</b>	More organized band near the impact-facing zone; limited downward extension.	Continuous, symmetric ring around the interface; stable and evenly redistributed stresses.

**Table 7.2:** Step time and number of degeneracy curves for feather and nylon shuttle corks across pre-impact, impact, and post-impact frames.

Time Frame	Feather Step Time	Feather Degeneracy Count	Nylon Step Time	Nylon Degeneracy Count
<b>Pre-Impact</b>	0.2	1412	3.75	2013
<b>Impact</b>	0.4	972	4.5	1416
<b>Post-Impact</b>	0.6	972	5.25	1462

## **8. Conclusion**

The study presented in this project focused on the numerical investigation of the impact behavior of feather and nylon badminton shuttles using finite element methods. The simulations were designed to capture the transient deformation, energy transfer, and rebound characteristics of each model under gravity-driven free fall conditions. The results obtained from explicit dynamic analyses provided an in-depth understanding of how material composition, geometry, and contact interactions influence shuttle performance, energy dissipation, and post-impact recovery.

### **8.1 Summary of Findings**

The mechanical response of each shuttle type was found to depend strongly on its material constitution and the corresponding energy transfer mechanisms during impact. The variation in internal and kinetic energies, rebound heights, and bounce angles confirmed that both feather and nylon shuttles behave distinctly under identical loading conditions.

#### **8.1.1 Feather Shuttle**

The feather shuttle demonstrated a smooth and gradual decay in energy over multiple bounces. The first impact converted a large portion of kinetic energy into internal strain energy within the cork head and feather junctions. The stored energy was partially recovered in subsequent rebounds, resulting in lower but stable bounce heights. The progression of impacts revealed that the shuttle maintained its structural in-

tegrity while exhibiting controlled deformation and consistent rebound motion.

The measured rebound heights decreased sequentially from approximately 10.7 mm after the first impact to 3.7 mm by the fifth impact. This steady decline in bounce height was accompanied by a corresponding decrease in bounce angle from 90 degrees to 58 degrees, indicating progressive rotational instability as energy dissipated. These results suggest that the natural anisotropy of feather material contributes to efficient energy absorption and controlled release, producing a realistic flight behavior that is desirable in professional play.

While the feather shuttle showed superior elasticity and controlled rebound, it also demonstrated a limited lifespan. The fine feather vanes and their adhesive joints are prone to fatigue and fracture after repeated impacts. The high cost of production, resulting from manual assembly and material sensitivity, further restricts its large-scale use. Nevertheless, its aerodynamic precision, stable orientation recovery, and smooth energy transition make it the preferred choice for professional tournaments where precision and responsiveness are prioritized over durability.

Beyond the rebound behavior, the tensor-field analysis provided additional insight into how the feather shuttle manages internal stresses during impact. The degeneracy curves concentrated around the feather–cork junction showed that stress directions reorganize rapidly in this region, reflecting the localized bending and shear transmitted through the feather roots. As the shuttle transitions from impact to rebound, these curves became more coherent and extended deeper into the cork, illustrating how the internal stress field redistributes as energy is absorbed and partially recovered. This pattern supports the observed rebound characteristics, showing that the feather–cork interface plays a key role in directing load and controlling deforma-

tion during each bounce.

### 8.1.2 Nylon Shuttle

The nylon shuttle, composed of a polymer skirt and a cork-based head, displayed a different energy response. The simulation revealed that the first impact produced a higher rebound height than the feather shuttle, reaching approximately 12.3 mm. This greater restitution during the first bounce can be attributed to the uniform geometry and stiffness of the polymer skirt, which momentarily stores and releases energy through elastic deformation. However, subsequent bounces showed a rapid decay in rebound height and energy amplitude, stabilizing by the third impact.

The kinetic and internal energy histories confirmed that the nylon shuttle dissipates a large portion of impact energy rather than structural recovery. The internal energy curve exhibited sharp peaks that decayed rapidly after each contact, indicating high energy absorption within the polymer matrix. The bounce angles for the nylon shuttle decreased gradually from 90 degrees to 82 degrees across three rebounds, suggesting that the shuttle maintained a stable orientation during rebound despite. This reflects its inherent structural consistency and resistance to excessive rotational motion.

The nylon shuttle proved to be more durable and stable under repeated loading. Its structure allows it to withstand numerous impacts without significant material degradation. The manufacturing process is also more economical, resulting in lower production costs. These features make the nylon shuttle suitable for training, recreational, and indoor use, where endurance and cost-efficiency are more critical than flight precision.

The tensor-field visualizations further supported these observations by showing that the nylon shuttle develops a broader and more uniform distribution of degeneracy curves around the skirt–cork interface during impact. The molded polymer geometry channels stress smoothly into the cork, producing continuous planar and linear degeneracies that lack the sharp clustering seen in the feather shuttle. After contact, these curves extend inward in a steady, symmetric pattern, indicating that the nylon structure spreads impact forces more evenly and reorganizes its internal stress field without abrupt directional shifts. This smoother redistribution of stresses aligns with the shuttle’s stable rebound behavior and its tendency to dissipate rather than recover energy during repeated impacts.

## 8.2 Comparative Discussion

The comparative analysis of both shuttles reveals distinct trade-offs between performance, durability, and cost. The feather shuttle offers superior energy recovery and realistic flight behavior but has limited endurance. Its lower bounce height and gradual decay in rebound reflect a more controlled energy release, consistent with the needs of high-level play. In contrast, the nylon shuttle achieves a higher initial bounce due to its stiffer structure but experiences faster energy dissipation. This leads to reduced rebound after the second or third bounce.

The correlation between simulation results and practical performance highlights that feather shuttles are optimized for precise aerodynamic control and energy transfer efficiency, while nylon shuttles are engineered for structural reliability and repeated use. The energy and bounce analyses confirm that the mechanical energy behavior of each shuttle directly relates to its market positioning and cost. Feather

shuttles are more expensive due to their material composition and labor-intensive construction, whereas nylon shuttles provide a lower-cost alternative that balances endurance and usability.

From the tensor-field perspective, the degeneracy curves further emphasize these differences. In the feather shuttle, the curves form concentrated clusters around the feather–cork junction, indicating localized stress redirection and controlled deformation during impact. The nylon shuttle, by contrast, exhibits broader and more uniform degeneracy patterns around the skirt–cork interface, reflecting smoother stress distribution and a tendency to dissipate impact energy rapidly. These structural signatures reinforce the observed rebound and energy trends, illustrating how each shuttle’s geometry and material composition shape its internal stress pathways during impact.

### 8.3 Overall Conclusion and Future Scope

In conclusion, the feather shuttle demonstrates the highest mechanical fidelity and energy efficiency, producing a refined impact response that aligns with professional standards. The nylon shuttle, however, delivers greater durability, stability, and cost advantage, making it the preferred option for non-professional and training applications. The higher first-bounce height observed in the nylon shuttle does not imply superior performance but rather reflects its elastic recovery.

The findings from this study establish a clear connection between shuttle material properties, energy dissipation mechanisms, and functional suitability. The analysis confirms that mechanical energy distribution, rebound consistency, and material behavior can serve as reliable indicators of shuttle quality and intended use. The

tensor-field visualizations further strengthened these observations by revealing distinct patterns in internal stress organization: the feather shuttle exhibited localized degeneracy clusters near the feather–cork junction, whereas the nylon shuttle displayed smoother, more uniformly distributed degeneracy curves around the skirt–cork interface. These structural signatures helped explain the contrasting rebound behaviors and the different ways each shuttle manages impact-induced deformation.

A promising direction for future research involves the development of hybrid shuttle designs that combine the elastic recovery of feathers with the durability of polymers. Such a configuration would allow the creation of an optimized shuttle that delivers both superior flight behavior and extended service life, potentially reducing the cost–performance gap between professional and recreational play.

This work demonstrates how finite element modeling can serve as a predictive and diagnostic tool for understanding shuttle dynamics and guiding the design of next-generation sports equipment that blends performance with sustainability.

## 8.4 Application: VR Badminton Game

To explore how the results from this study can support interactive analysis and training tools, a virtual reality badminton environment was developed using Unity and SteamVR. The aim of this game was to demonstrate how the mechanical behavior captured in the finite element simulations can guide real-time shuttlecock motion inside an interactive graphics engine. The workflow began by creating a scaled badminton court inside Unity and importing the shuttlecock geometry originally prepared for the finite element model. Using the same geometry ensured that the visual representation and spatial proportions in VR remained consistent with the physical model

used in the simulations.

SteamVR was integrated into the Unity project to enable full six-degree-of-freedom tracking of both the headset and controllers. This allowed the user to stand on the virtual court, move freely within the tracked area, and interact with the shuttle using natural hand and arm motion. A set of custom C# scripts was written to manage shuttle motion, racket interaction, and overall gameplay. One script used velocity trends, rebound height ratios, and orientation changes derived from the FEM results to drive the shuttle behaviour after each impact. Another script measured the instantaneous velocity of the virtual racket and updated the shuttle trajectory whenever the user performed a swing. Additional scripts handled point detection, game resets, and interaction events involving the floor, boundaries, and the racket.

## Unity-based Setup

The Unity environment was constructed using a standard 3D URP (Universal Render Pipeline) template, with the badminton court modeled at full scale based on BWF dimensions. Lighting, colliders, and physics layers were configured to ensure consistent interaction between the racket, shuttle, and ground plane. The imported shuttlecock geometry was simplified for real-time use while preserving the external silhouette that defines aerodynamic motion in VR. The FEM-derived kinematic response curves were then encoded as lookup tables within the C# scripts, allowing Unity's physics engine to approximate the rebound angles and velocity decay without solving structural deformation in real time. The overall setup provides a responsive environment while remaining computationally inexpensive for consumer headsets.

## **VR System and Interaction**

The VR system was built using the SteamVR plugin, which provides controller tracking, input mapping, and headset pose updates. The game was tested using the HTC Vive Pro 2, although the implementation is device-independent and can be run on any SteamVR-compatible headset. Controller poses were mapped directly to a virtual racket model, allowing the user to swing naturally inside the virtual court. The collision system was tuned so that only specific parts of the racket trigger a shuttle response, mirroring real impact behavior and preventing unrealistic interactions.

## **User Experience and Gameplay**

From a user perspective, the VR environment operates like a simplified practice court. After wearing the headset, the player finds themselves positioned at the center of a regulation-sized court with a racket in hand. The shuttle is launched with an initial velocity and orientation, and the user can perform forehand and backhand swings to keep it in play. Each impact triggers an updated trajectory computed using the FEM-informed motion rules, reflecting the progressive loss of kinetic energy that causes the shuttle’s rebound height and post-impact motion to diminish over time. Although the game does not attempt to simulate feather deformation or skirt flexure in real time, it captures the overall behaviour and impact response observed in the simulations. This creates an immersive experience in which the shuttle “feels” believable during play.

Overall, this application demonstrates how high-fidelity mechanical simulations can support the development of physics-informed visualization tools and interactive training environments. It also shows a potential path for integrating finite

element results with real-time graphics engines for sports engineering, virtual prototyping, and performance analysis.

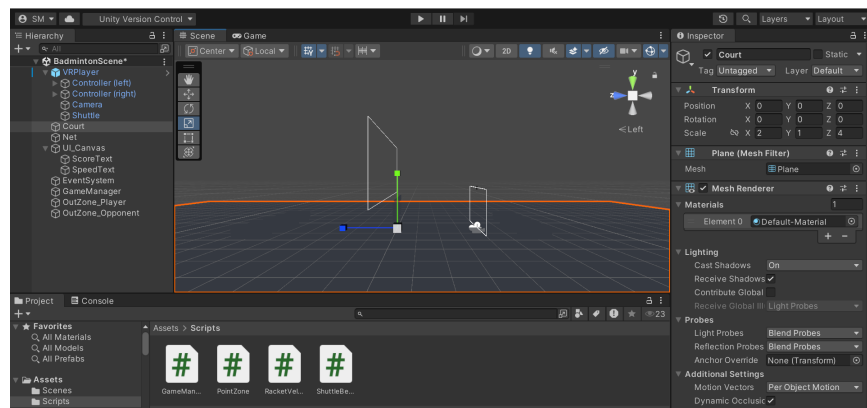
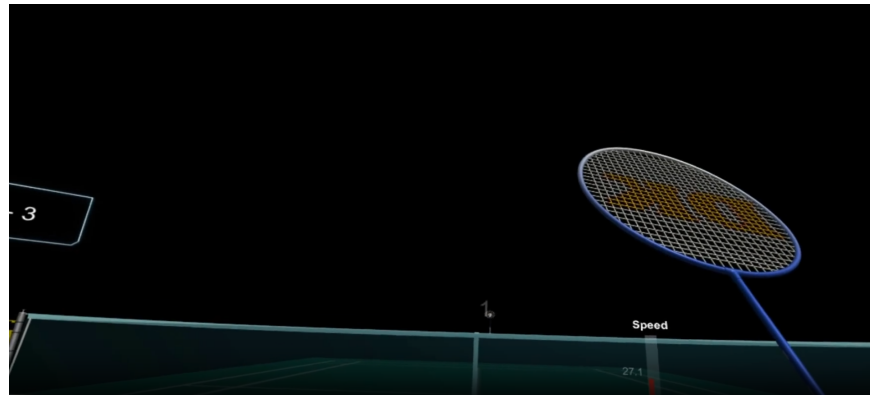


**Figure 8.1:** Frames from the developed VR badminton environment showing in-game interaction and Unity-based scene setup.

## References

1. K.-J. Bathe, *Finite Element Procedures*. Prentice Hall, 2006.
2. O. C. Zienkiewicz, R. L. Taylor, and J. Z. Zhu, *The Finite Element Method: Its Basis and Fundamentals*, 7th ed. Butterworth–Heinemann, 2013.
3. T. Belytschko, W. K. Liu, B. Moran, and K. Elkhodary, *Nonlinear Finite Elements for Continua and Structures*, 2nd ed. Wiley, 2013.
4. R. D. Cook, D. S. Malkus, M. E. Plesha, and R. J. Witt, *Concepts and Applications of Finite Element Analysis*, 4th ed. Wiley, 2002.
5. J. N. Reddy, *An Introduction to the Finite Element Method*, 3rd ed. McGraw–Hill, 2006.
6. J. Fish and T. Belytschko, *A First Course in Finite Elements*. Wiley, 2007.
7. Y. Zhang and C. Bajaj, “Adaptive and quality quadrilateral/hexahedral meshing from volumetric data,” *Computer Methods in Applied Mechanics and Engineering*, vol. 217–220, pp. 131–150, 2018.
8. P. Wriggers, *Computational Contact Mechanics*, 2nd ed. Springer, 2006.
9. K. L. Johnson, *Contact Mechanics*. Cambridge University Press, 1985.
10. S. E. Benzley, E. Perry, K. Merkley, B. Clark, and G. Sjaardema, “A comparison of all hexagonal and all tetrahedral finite element meshes for elastic and elastic–plastic analysis,” *Proceedings, 4th International Meshing Roundtable*, pp. 179–191, 1995.

11. R. W. Ogden, *Non-Linear Elastic Deformations*. Dover Publications, 1997.
12. M. Mooney, “A theory of large elastic deformation,” *Journal of Applied Physics*, vol. 11, no. 9, pp. 582–592, 1940.
13. O. H. Yeoh, “Some forms of the strain energy function for rubber,” *Rubber Chemistry and Technology*, vol. 66, no. 5, pp. 754–771, 1993.
14. J. O. Hallquist, *LS-DYNA Theory Manual*. Livermore Software Technology Corporation, 2006.
15. Dassault Systèmes, *Abaqus 2024 Documentation*. SIMULIA, 2024.
16. Siemens Digital Industries Software, *Simcenter Nastran and NX Documentation*. Siemens, 2023.
17. R. Cross and J. Lindsey, “Impact of a ball with a tennis racket: a finite element approach,” *Sports Engineering*, vol. 13, no. 2, pp. 69–76, 2011.
18. J. E. Goff, *Gold Medal Physics: The Science of Sports*, 2nd ed. Johns Hopkins University Press, 2016.
19. T. Yeo, P. K. Chua, and H. T. Low, “Numerical simulation of shuttlecock aerodynamics,” *Procedia Engineering*, vol. 2, no. 2, pp. 2435–2440, 2009.
20. ASTM International, *ASTM D412-16: Standard Test Methods for Vulcanized Rubber and Thermoplastic Elastomers—Tension*. ASTM, 2016.
21. G. R. Liu and S. S. Quek, *The Finite Element Method: A Practical Course*, 2nd ed. Butterworth-Heinemann, 2008.

22. G. A. Holzapfel, *Nonlinear Solid Mechanics: A Continuum Approach for Engineering*. Wiley, 2000.
23. K.-J. Bathe and E. Noh, “Insight into an implicit time integration scheme for structural dynamics,” *Computers & Structures*, vol. 85, no. 7–8, pp. 437–445, 2007.
24. R. Cooke, “Mechanical response of composite racket structures,” *Journal of Sports Engineering and Technology*, vol. 211, no. 2, pp. 97–106, 1997.
25. S. Ramesh and D. K. Rajan, “Dynamic response of badminton shuttlecock under impact loading using finite element simulation,” *Materials Today: Proceedings*, vol. 18, pp. 532–540, 2019.
26. Blender Foundation, *Blender 3.x Manual*. The Blender Foundation, 2024.
27. I. M. Daniel and O. Ishai, *Engineering Mechanics of Composite Materials*, 2nd ed. Oxford University Press, 2006.
28. G. R. Liu and S. S. Quek, “A practical introduction to finite element methods,” Butterworth–Heinemann, 2014.
29. A. Shah, Y. Chauhan, P. Patel, and B. Chaudhury, “Multivariate-data-visualization-based investigation of projectiles in sports,” *European Journal of Physics*, vol. 39, no. 4, p. 044001, 2018. doi:10.1088/1361-6404/aab585.